

1 **The anatomy of exhumed river-channel belts: Reconstructing bedform- to belt-scale river**
2 **kinematics from the Cretaceous Cedar Mountain Formation, Utah, USA**

3 Benjamin T. Cardenas^{1*}, David Mohrig¹, Timothy A. Goudge¹, Cory M. Hughes², Joseph S. Levy³,
4 Travis Swanson⁴, Jasmine Mason¹, and Feifei Zhao¹

5 ¹Jackson School of Geosciences, University of Texas at Austin, Austin, TX, USA

6 ²Department of Geology, Western Washington University, Bellingham, WA, USA

7 ³Department of Geology, Colgate University, Hamilton, NY, USA

8 ⁴Department of Geology and Geography, Georgia Southern University, Statesboro, GA, USA

9

10 *Corresponding Author Contact Information

11 Telephone: (210) 240-0382

12 Email: benjamin.cardenas@utexas.edu

13

14 Submitted to Sedimentology on August 29th, 2019

15 **THIS IS A NON-PEER REVIEWED PRE-PRINT**
16 **SUBMITTED TO EARTHARXIV AND UNDER REVIEW**
17 **AT SEDIMENTOLOGY**

18 Word Count: 7,792 (Title, authors, affiliations, main text except refs & captions, 8,000 limit)

19 Abstract: 300 (300 word limit)

20 Pages: 41

21 Figures: 22

22 References: 88

23 ABSTRACT

24 The geometry of river-channel belts is shaped by the migration, aggradation, and
25 avulsion of associated rivers, which is controlled by the motion of bedforms and barforms. The
26 motion of bedforms and barforms can be reconstructed using the geometry and preservation of
27 their associated strata. In order to reconstruct the kinematics of the ancient Cedar Mountain
28 rivers, preserved elements of the formative river channels, including bars, planform geometry,
29 and bed topography, are measured within exhumed fluvial strata exposed as ridges in the
30 Cretaceous Cedar Mountain Formation, Utah, USA. High-resolution ortho-images created by
31 Uncrewed Aerial Vehicles facilitated geologic field mapping, as were vertical and lateral
32 sections. The studied ridges are compound structures composed of the stacked deposits of
33 multiple, individual channel belts representing at least 5 to 6 channel re-occupations. Lateral
34 sections reveal sets of dune cross-beds constructing well-preserved barforms. Locally, the
35 paleo-topography of paleo-barforms defines the modern topographic surface of the outcrop.
36 Comparison of the channel-belt centerline to local paleotransport directions indicate channel
37 planform morphology was preserved through multiple re-occupations and minimal lateral
38 migration. The preservation of these formative channel elements is the product of the
39 kinematics of the depositional system. The avulsive character of the system preserved the state
40 of the active channel bed and its individual bars at the time of channel switching. Calculated
41 sedimentation durations for the preserved elements vary within a belt from a day to 11 days,
42 indicating most of the time recorded in these compound channel belts is represented by the
43 basal erosional surfaces at the bottom of channel belts. Avulsions in this system were frequent
44 with respect to lateral migration rates, which minimized lateral channel amalgamation. The

45 well-preserved belts may be indicative of a larger-scale topography driving sedimentation at
46 the belt scale, much as bar topography can locally increase dune sedimentation rates and
47 preservation.

48 Keywords: fluvial sedimentology, channel belt, preservation, bar, sinuous ridge

49

50 **INTRODUCTION**

51 Fluvial channel belts are the time-integrated, channel-filling deposits of rivers. These
52 channel-filling deposits include strata associated with bedforms, such as ripples and dunes, as
53 well as free and forced bars. The vertical and lateral motion of a river is recorded by the motion
54 of these bedforms and bars, which in turn control the geometry of the resultant channel-belt
55 deposits and drive the belt's geometry away from that of the formative river (Van De Lagewag
56 et al., 2013). Therefore, in order to determine how ancient rivers migrated, aggraded, and
57 avulsed, it is necessary to understand the accumulation and preservation of the bedform and
58 barform strata within the associated channel belts (e.g., Reesink et al., 2015; Durkin et al.,
59 2018; Paola et al., 2018; Chamberlin and Hajek, 2019).

60 This work examines an erosionally exhumed, laterally and vertically amalgamated
61 complex of fluvial channel belts in the Cretaceous Cedar Mountain Formation, Utah, USA (Fig.
62 1). The goal of the project is to determine what aspects of ancient river topography and
63 geometry are partially-to-fully preserved within the channel belts. Paleo-environmental
64 properties such as water and sediment discharge associated with an ancient fluvial system can

65 be quantitatively estimated using geometric properties of its paleo-channels, if these
66 geometries can be accurately estimated from deposits representing the time-integrated record
67 of channel motion, deposition, and erosion (Wright and Parker, 2003; Parker et al., 2007;
68 Hayden et al., 2019). Here, new methodologies are developed for extracting the river-channel
69 kinematics from channel-belt deposits so that the most accurate picture of the formative paleo-
70 river channel and its kinematics, from bedform to planform scale, can be established. For
71 example, were these belts produced during incremental sedimentation, or do they represent a
72 snapshot of the channel topography and geometry at the time of avulsion? This topography
73 includes bed topography, such as barforms and bedforms, as well as planform channel
74 geometry. The measurements presented here cover the channel belts across a range of scales,
75 from local stacks of cross sets to the entirety of the outcrop, in order to understand the river
76 system that produced Cedar Mountain. The datasets analyzed in this work include aerial images
77 collected from a remotely piloted aircraft systems (RPAS, or “drone”), field maps, vertical and
78 lateral sections, modern river analogs, and another ancient example of fluvial stratigraphy in
79 the nearby Jurassic Morrison Formation. These methods and results provide a comparative
80 baseline for future studies of fluvial channel belts and their associated ancient fluvial systems.
81 The reconstruction of bed aggradation rates using these methods will also further the
82 community’s understanding of how time in the rock record is recorded by preserved strata
83 versus erosional surfaces (Sadler, 1981; Paola et al., 2018).

84

85 **Background**

86 *Cedar Mountain Formation*

87 The rivers associated with the deposition of the lower Cretaceous Cedar Mountain
88 Formation drained uplifted areas of modern-day western Utah northeastward into the Mowry
89 Sea and its successor, the Western Interior Seaway. Ultimately, basin subsidence led to the
90 burial of the Cedar Mountain Formation by late Cretaceous coastal and marine deposits of the
91 Dakota Sandstone and the Mancos Shale (Currie, 1998). A regional unconformity separates the
92 base of the Cedar Mountain Formation from the top of the upper Jurassic Morrison Formation
93 (Peterson and Ryder, 1975; Kowallis et al., 1986). The Cedar Mountain Formation has been
94 interpreted as consisting of river channel-filling sandstones and conglomerates, and overbank
95 mudstones and paleosols (Stokes, 1961; Currie, 1998; Garrison et al., 2007; Nuse, 2015; Hayden
96 et al., 2019).

97 Much of the recent work regarding the Cedar Mountain Formation has focused on the
98 geomorphology of exhumed channel-filling deposits. The channel belts are more resistant than
99 the surrounding floodplain material, resulting in the preferential erosion of floodplain strata
100 and preservation of the channel fill which defines the modern topography (Williams et al.,
101 2007; 2009; Hayden et al., 2019). The landscape within the eroding Cedar Mountain is defined
102 by ridges as tall as 35 m and 60 to 90 m wide on average, composed of exhumed channel belts
103 that are exposed in three dimensions (Fig. 1). Recent interest in these landforms and other
104 exhumed channel fills (e.g., Hayden et al., 2019; in Oman, Maizels 1987, 1990; Maizels and
105 McBean, 1990; in Egypt, Zaki et al., 2018) has partially been driven by high-resolution images of
106 morphologically similar 'fluvial sinuous ridges' on Mars (e.g., Burr et al., 2009; Davis et al., 2016;

107 Cardenas et al., 2018; Hughes et al., 2019). Hayden et al. (2019) have provided an important
108 comparison between field- and remote-sensing-based paleo-hydraulic reconstructions for the
109 Cedar Mountain Formation ridges, but a detailed sedimentologic workup provides additional
110 information for any paleo-environmental analysis.

111

112 *Dune, bar, and channel belt strata*

113 The dip direction of a dune cross stratum records the orientation of the formative dune
114 lee face, and reflects local dune migration direction (Allen, 1970; Rubin and Hunter, 1982). This
115 relationship is complicated for dunes with sinuous crestlines and variably deep troughs, which
116 create trough cross-stratification (McKee and Weir, 1953; DeCelles et al., 1983; Rubin, 1987).
117 Because of the crestline sinuosity, the local dip direction of a set of trough cross-stratification
118 may represent the mean migration direction of the associated dune plus or minus as much as
119 90° (Dott Jr., 1973). In plan-view exposures where local variability in individual dune cross strata
120 can be seen within the context of an entire set, the central axis of the set of trough-cross strata
121 can be clearly seen and migration direction can be unambiguously determined (Dott Jr., 1973).

122 Dipping strata composed of superimposed sets of dune cross strata represent the
123 accretion surfaces of larger-scale barforms. In active rivers, barforms are either forced by
124 channel shape or are free to migrate downstream (Miall, 1977; Seminara and Tubino, 1989;
125 Ikeda, 1989; Hooke and Yorke, 2011). Bars fixed to the inner bank of a channel bend, i.e., point
126 bars, grow into the channel (Ikeda et al., 1981) and record lateral river migration. Point bars
127 have been identified in the rock record based on sigmoidal lateral accretion surfaces dipping at

128 approximately perpendicular angles to the local dip directions of dune cross strata (e.g.,
129 Edwards et al., 1983; Wu et al., 2015; Almeida et al., 2016). Free bars may preserve a wider
130 array of relationships between local dune migration direction and the bar surface dip direction
131 (e.g., Allen, 1983; Almeida et al., 2016). Although not often discussed in the literature, free bars
132 and forced (point) bars commonly coexist in channels (Fig. 2; Kinoshita and Miwa, 1974;
133 Whiting and Dietrich, 1993; Hooke and Yorke, 2011).

134 In net-depositional settings, aggradation of the riverbed is coupled with aggradation of
135 the channel margins that exceeds distal floodplain aggradation (Pizzuto, 1987). Over time, the
136 channel becomes elevated relative to the floodplain, and the difference between the two
137 elevations defines the channel's superelevation. Past studies have shown that a superelevation
138 of 60% of the flow depth appears to be a threshold for river avulsion (Mohrig et al., 2000), the
139 process by which flow abandons a channel in favor of a lower topographic position (Heller and
140 Paola, 1996; Mohrig et al., 2000; Hajek and Edmonds, 2014). Studies of both modern and
141 ancient avulsive rivers suggest that rivers tend to return to previously abandoned channels that
142 became gravitational attractors to flow following the aggradation of the adjacent floodplain
143 (Heller and Paola, 1996; Reitz et al., 2010; Edmonds et al., 2016). Such systems leave behind
144 channel-belt complexes, i.e., sedimentary deposits composed of stacked channel-belts (Friend,
145 1979; Mohrig et al., 2000; Jones and Hajek, 2007; Cuevas Martínez et al., 2010; Chamberlin and
146 Hajek, 2015; Hayden et al., 2019).

147

148 **METHODS**

149 **Field campaign**

150 For this study, several datasets were acquired during a field campaign at two ridges
151 formed from exhumed fluvial strata of the Ruby Ranch Member of the Cedar Mountain
152 Formation (Fig. 1A and B). Aerial photosurveys, collected with a DJI Phantom 2 Vision Plus
153 drone, imaged the top and side surfaces of both ridges with >75% along path and side overlap
154 in photos (Fig. 1C-D). Flights were conducted from 15 to 20 m above ground level (AGL). Ground
155 control point locations were determined using an Archer Field PC with an external GPS antenna,
156 producing horizontal position data with <0.3 m RMS accuracy. Orthophotomosaics were
157 generated with 5 cm spatial resolution and were orthorectified using the concurrently
158 produced digital elevation model (DEM) using Agisoft Photoscan Pro [It's customary to cite the
159 agisoft website for this]. Structure from DEMs and orthoimages cover an area of 0.213 km² over
160 the eastern and western ridges (Fig. 1C to D). These datasets were used to map the locations of
161 bounding surfaces of cross-sets of various scales and major erosional surfaces. Dip directions of
162 cross-strata identified on the photomosaics were measured in the field using compasses.
163 During this survey, each set was classified as either being composed of sandstone or
164 conglomerate.

165 In addition to the plan view data, several sets of vertical sections were logged. Around
166 the perimeters of each ridge, 59 vertical sections were measured covering the entirety of the
167 available vertical exposure of the ridge-capping rock, resulting in 276 total meters of section.
168 Collecting the thicknesses of units between major bounding surfaces was the primary goal of
169 this effort. An additional 31 two dimensional (2-D) panels ranging from 1 m to 10 m wide were

170 collected around the perimeters of both ridges in order to describe the smaller, cross-set scale
 171 architectural elements of the channel belts. Architectural variability in the transport direction at
 172 the scale of a few meters was recorded, including changes in set thickness and the dips of
 173 bounding surfaces. Across all of these surveys, the thickness of 362 sets of cross strata were
 174 measured, and grain size was measured for 75 of those sets in the field using a grain size card.
 175 Using a geographic information system (GIS), field mapping results were merged with the
 176 remote sensing measurements. Ridge-scale bounding surfaces were digitized as lines, and 1,071
 177 sets of planform-exposed trough cross strata and 107 exposures of large-scale dipping strata
 178 were digitized as polygons.

179

180 **Modern analogs and the transport anomaly**

181 To test how well the ridge outcrop centerlines represent original channel centerlines, a
 182 metric named here as the transport anomaly, θ_{TA} , is defined for both modern rivers and the
 183 exhumed channel fills.

$$184 \quad \theta_{TA-CHANNEL} = \theta_{CL-CHANNEL} - \theta_{D-CHANNEL} \quad (1a)$$

$$185 \quad \theta_{TA-RIDGE} = \theta_{CL-RIDGE} - \theta_{D-RIDGE} \quad (1b)$$

186 where θ_D is the 0 – 359° orientation of a transport or paleotransport measurement from an
 187 active dune ($\theta_{D-CHANNEL}$; Eq. 1a) or cross set ($\theta_{D-RIDGE}$; Eq. 1b), and θ_{CL} is the orientation of the
 188 centerline nearest to the location where θ_D was measured (Fig. 3). Values of θ_{TA} may be
 189 positive or negative, and are calculated using the Circular Statistics Toolbox available for

190 MATLAB, which measures the shortest angular distance, positive or negative, between the two
191 directions such that no measurement exceeds 180° or is less than -180° (Berens, 2009).

192 By measuring $\theta_{D-CHANNEL}$ from dunes in modern rivers and $\theta_{TA-RIDGE}$ from planform-
193 exposed cross sets in the Cedar Mountain, hundreds of measurements of θ_{TA} (Eq. 1a to b)
194 between the ancient and modern systems were compared to test whether the transport
195 anomalies for the Cedar Mountain outcrop is systematically distinct from transport anomalies
196 observed in a modern river system, which in turn is used to understand how well the
197 centerlines of formative Cedar Mountain rivers are preserved in the exhumed channel belts and
198 represented by ridge geometry (Fig. 4A and B). For example, if the mean and standard deviation
199 (σ) of $\theta_{TA-RIDGE}$ (Eq. 1b) approximately equal those of $\theta_{TA-CHANNEL}$ (Eq. 1a), then the transport
200 anomaly of the Cedar Mountain is no greater than the variability in a modern river, and is
201 consistent with ridge planform preserving the formative channel planform (Fig. 4A). If lateral
202 migration and reworking has greatly widened the belt and reduced its overall sinuosity from
203 that of the formative channels, σ should be greater in the Cedar Mountain, as well as a more
204 random distribution of $\theta_{TA-RIDGE}$ (Fig. 4B). An example of the latter case comes from visual
205 inspection of point bar strata of the Ferron Sandstone in Wu et al., (2015, their Fig. 13; 2016,
206 their Fig. 8), which shows a general northwest-curving paleotransport trend along a northeast
207 trending exposure, making their study location a high paleo-transport anomaly zone. Note that
208 the deviation angle in Wu et al. (2016) is calculated relative to an interpreted channel-form, not
209 the exhumed channel-belt shape. Wang and Bhattacharya (2017) show a more pronounced
210 example linked to point bar growth in their Figure 10A. Durkin et al. (2018) show examples of
211 this lateral amalgamation in ancient (McMurray Formation) and the modern (Mississippi and

212 New Madrid Rivers). In a third scenario where erosion patterns have not exhumed the belt
213 evenly from all directions, neither of the prior scenarios would be observed.

214 Measurements from active dune fields in a braided reach of the North Loup River,
215 Nebraska, USA, and the meandering Trinity River, Texas, USA, were used as the comparative
216 modern systems in this analysis. The North Loup is a sand bed river that has been used as a
217 modern analog to ancient fluvial strata (Mohrig et al., 2000; Mahon and McElroy, 2018). A UAV
218 photomosaic collected by Swanson et al. (2018) was used that images a 760 m reach of the
219 river in which downstream migrating bars and dunes, as well as the channel banks, are clearly
220 identifiable. The evolution of the Trinity River has recently been studied in detail using
221 topographic and bathymetric datasets (Mason and Mohrig, 2019; in review). These datasets
222 provide 32 river km to map dune crests on the river bed, as well as dunes formed during
223 bankfull flow and currently stranded on subaerially-exposed point bar surfaces.

224 Points defining the centerlines of each river were calculated using the series of points
225 defining each channel bank. For each point on one bank, the distance to the nearest point on
226 the opposite bank is calculated and taken as a local width measurement, and a centerline point
227 is placed at the location exactly between the two points. The North Loup banks, and therefore
228 the centerline, are defined by points spaced about 1 m apart, approximately that of a
229 representative dune wavelength in the North Loup River (Swanson et al., 2018). In a GIS, the
230 brink lines of 2,871 dunes covering a 763-m reach of the river were mapped using an
231 orthorectified UAV photomosaic. The orientation of each dune was estimated by a best-fit line
232 to a series of mapped brink points. The normal to each brink line, in turn, was taken as the local

233 transport direction for that dune, $\theta_{D-CHANNEL} \cdot \theta_{D-CHANNEL}$ was then tied to a point located at the
234 average XY coordinate of all XY coordinates defining that particular dune brink line.

235 The same process was applied to 2,190 bedforms over the imaged 32 km reach of the
236 Trinity River imaged using sonar profiles of dunes on the channel bed (dataset from Mason and
237 Mohrig, in review), as well as dunes frozen on subaerially exposed point bar surfaces formed
238 during the previous bankfull flood imaged in a 2015 lidar survey (Mason and Mohrig, 2018).

239 In the Cedar Mountain, ridge centerlines were calculated using mid-points between the
240 left- and right-hand ridge edges, and smoothed using a spline method in the MATLAB curve
241 fitting toolbox. Centerlines are ultimately defined as points spaced ~1 m apart along the
242 smoothed line. Ridge width was measured at 10 m intervals along the centerline. Values for θ_{D-}
243 $RIDGE$ are taken from field measurements of planform trough cross strata across the top surfaces
244 of the two ridges ($n = 1,071$), and assigned associated XY coordinates at the center of the
245 corresponding mapped set.

246

247 **RESULTS**

248 **Vertical sections**

249 The measured vertical sections from around the perimeters of each ridge were
250 composed of over 99% cross-stratified sandstones and conglomerates. Where mudstones are
251 incorporated within the vertical sections they are associated with ridge-scale erosional surfaces,
252 and have thicknesses that range from pinched out to a maximum of 0.60 m. Mudstone

253 thickness can vary over short, meters-scale distances due to erosion from overlying channel
254 elements, but the erosional surfaces these mudstones were deposited on top of are laterally
255 persistent across ridges. These persistent erosional surfaces are used to define and separate
256 individual channel-belt stories (Fig. 5A and B and 6A and B; Friend et al., 1979). Any given
257 vertical section exposes one to four stacked stories which locally vary in thickness from 0.10 m
258 to 8.60 m, with a mean of $3.10 \text{ m} \pm 0.22 \text{ m}$ (the calculated standard error of the mean), median
259 of $2.80 \text{ m} \pm 0.27 \text{ m}$ (the calculated standard error of the median) and σ of $2.03 \text{ m} \pm 0.15 \text{ m}$ (the
260 calculated standard error of the standard deviation; $n = 89$; Fig. 6C). These story-bounding
261 surfaces are also exposed along the top surfaces of the ridges. Five of these surfaces have been
262 mapped across the western ridge, and four have been mapped across the eastern ridge (Fig.
263 5C).

264

265 **Sedimentary structures and architecture**

266 The most common sedimentary structures preserved in plan view and vertical
267 exposures of the Cedar Mountain Formation ridges were trough cross sets (Fig. 7A to D) with
268 median grain sizes ranging from upper-fine sand to medium pebbles (Fig. 8A to C). The mean
269 thickness of these sets was $0.12 \text{ m} \pm 0.005 \text{ m}$, with a standard deviation of $0.09 \text{ m} \pm 0.003 \text{ m}$,
270 and a coefficient of variation of 0.79 ± 0.04 ($c_v = \sigma/\text{mean}$, with propagated errors; $n = 350$).
271 Along the top ridge surfaces where these structures were exposed and mapped in plan view
272 (Fig. 9), the dominant dip direction of these sets was clearly identified and representative of the
273 associated bedform's migration direction. The polygons outlining these planform exposed sets

274 (n = 1,071) sum to a total area of 5,019 m². Of the 1,071 sets mapped in planform, 269 were
275 identified as conglomerate, representing 25.1% of sets and 26.5% (1330 m²) of total set area.
276 The remaining 802 sets were identified as sandstone, representing 74.9% of sets and 73.5%
277 (3689 m²) of total set area. Larger scale thicker compound cross-sets (n = 12), with a mean of
278 1.28 m ± 0.05 m and a σ of 0.19 m ± 0.04 m measured at preserved rollovers, and are also
279 exposed in plan view (Fig. 10A-D). The locations of plan view measurements of both types of
280 sedimentary structures are shown in Figure 11. The summed planform exposure area of these
281 sets (n = 103) is 520 m², or covering 10.3% of the planform area of trough cross-sets. Within
282 individual channel belt stories, shingled trough cross-sets record transport up and down larger-
283 scale topography (Fig. 12A-D).

284 Four arrangements of cross sets were observed, and are referred to as Type A, B, C, and
285 D. Type A featured a thick basal set of compound strata scoured along its top by an upstream-
286 dipping surface, and overlain by a thinner coset composed of smaller cross sets with a mean
287 thickness and standard deviation of 0.12 m ± 0.01 m and 0.07 m ± 0.01 m (Fig. 13). The
288 upstream dips of the scour surface range from 5° to 13° (mean = 7°, n = 6). In this case,
289 orientation of small cross sets roughly parallel the dip direction of the larger cross sets.

290 Type B featured a thick basal set of compound cross-sets that change both dip and
291 thickness in the downstream direction (Fig. 14). Individual cross sets thickened by as much as
292 300% over 1.5 meters in the downstream direction (E.g. 0.08 m to 0.23 m, 0.07 m to 0.23 m,
293 and 0.06 m to 0.19 m). Correspondingly, the bounding surfaces separating these cross sets
294 shallow downstream from as steep as 26° to as shallow as 5°, and the upper bounding surface

295 transitions from being markedly erosional to conformable (Fig. 14). Similar to type A, the
296 smaller cross sets roughly parallel the dip direction of the larger cross sets. The mean thickness
297 and standard deviation of these sets at shallowly dipping sections were $0.13 \text{ m} \pm 0.01 \text{ m}$, and
298 $0.08 \text{ m} \pm 0.01 \text{ m}$, respectively.

299 Type C was also composed of compound strata, but in these cases the dip direction of
300 the smaller foresets were roughly transverse to the dip direction of the larger cross sets (Fig.
301 10D). Type C sets were identified in plan view exposures, so set thickness measurements were
302 not made. Strata composing Types A, B, and C are sandstones.

303 Type D featured no compound cross-stratification, and bounding surfaces were sub-
304 horizontal or showed local variable curvature associated with trough geometry. Type D strata
305 featured pebble conglomerates and a $\sim 90^\circ$ scatter of transport directions, apparent by the
306 juxtaposition of trough and dip-normal exposures (Fig. 15). The mean thickness and σ of type D
307 sets was $0.19 \text{ m} \pm 0.02 \text{ m}$ and $14.7 \text{ m} \pm 0.02 \text{ m}$, and sections contain up to ten stacked sets.

308

309 **Transport anomalies**

310 Maps of transport anomalies (θ_{TA}) for the Cedar Mountain Formation and North Loup
311 River are presented in Fig. 16A to C. The associated θ_{TA} histograms and statistical moments for
312 these systems and the Trinity River are presented in Figure 17A to D. Significantly, all datasets
313 have mean values ranging between -12° and $+6^\circ$, and standard deviations ranging from 25° to
314 35° . In the North Loup, anomalies were clearly controlled by local bar topography. However,

315 measured transport anomalies approach the reach mean when assembled over a downstream
316 distance of ~3 bar lengths (Figs. 16C and 18A to C). In the Trinity, as expected for meandering
317 rivers, both the magnitude of the mean and standard deviation of the transport anomalies are
318 the smallest (Fig. 17D). Transport anomalies that are observed are largely due to the deflection
319 of flow obliquely down point bar surfaces (Dietrich and Smith, 1984). In the Cedar Mountain,
320 areas with concentrated high anomalies were found to be located at ridge bends (Fig. 16A to B).

321

322 **DISCUSSION**

323 **Dune, bar, belt, and overbank strata**

324 A distinction is drawn between cross sets on either side of the break in scale shown in
325 Figure 8A. The thinner-bedded trough cross strata (Fig. 7A to C) are interpreted as forming via
326 the migration of 3-D dunes with variably deep troughs (Rubin, 1987). In planform and vertical
327 sections, these are clearly distinct from larger-scale dipping strata (Fig. 10A to D), which do not
328 show the same bounding-surface curvature and, significantly, feature cross strata defined by
329 compound cross-sets (Figs. 10D and 14A and B). These larger-scale strata are interpreted as
330 accretionary river-bar deposits (Edwards et al., 1983). The population of dip direction vs.
331 centerline trend anomalies for the bar strata feature a larger spread of values and modes
332 situated far from zero (compare Fig. 17A to D against Fig. 17E to F). The range of values
333 suggests the formative bar types included point bars with primarily cross-stream accreting
334 surfaces (Fig. 10D), and free bars which can feature cross-stream-, downstream-, and upstream-
335 dipping accretion surfaces (Skelly et al., 2003). Point bar structures are best observed at the

336 ridge scale, where clusters of bar surfaces dip towards the convex sides of ridge bends (Fig. 11;
337 note that the western-most point bar strata define a convex-north bend, Fig. 1C). Together,
338 these dune- and bar-scale cross strata are interpreted as deposits filling river channels during
339 episodes of active sediment transport within that channel reach. The mudstones associated
340 with ridge-scale erosional surfaces are interpreted to represent sedimentation during periods
341 of channel abandonment, which indicates a system that experienced multiple avulsions and
342 channel reoccupations (Mohrig et al., 2000; Jones and Hajek, 2007; Cuevas Martínez et al.,
343 2010). However, not every reoccupation of a channel during avulsion preserves a mudstone
344 layer connected to the channel-belt boundary.

345 The four cross-stratal types observed in the Cedar Mountain ridges document the
346 interaction of the ancient dunes and bars. Type A architectures are characteristic of free bars,
347 and possess a bar-scale bounding surface, shown in red in Figure 13, separating bar lee strata
348 below from deposits of the bar stoss surface above. As such, this bounding surface preserves
349 the characteristic dip of the stoss side of the bar form. At first glance, it might seem surprising
350 to accumulate a coset of stoss-side deposits, but theory (Paola and Borgman, 1991) and a
351 recent morphodynamic bedform model (Swanson et al., 2019) show that set stacking can occur
352 even under conditions of net bypass and net erosion because of variability in dune scour
353 depths.

354 Type B architectures highlight change in compound dune strata imparted by free bar
355 migration (Fig. 14). The steepest 26° cross strata represent lee construction in a direction
356 approximately normal to average transport. The observed shallowing of bounding-surface dips

357 and thickening of sets in the downstream direction records the planform deformation of the
358 bar crest over time, where steep downstream-accreting surfaces gradually begin to accrete
359 laterally. As evident from the compound nature of these sets (Fig. 14), this bar growth is driven
360 by dune accretion in front of the bar. At the two locations where A and B type architectures are
361 adjacent (Figs. 13 and 14), the transition of the stoss scour surface to the conformable
362 bounding surface of a cross-stratum represents the delivery of sediment mined from the bar
363 stoss up and over the crest of the bar, and onto the bar lee. Taken together, these two
364 architectures preserve the processes associated with bar migration via the mining and delivery
365 of sediment by a surface veneer of smaller dunes compound to a larger free bar. These are the
366 'form sets' of Reesink et al. (2015), but observed in bar strata rather than dune strata. One
367 lateral section shows the stacking of lee strata on stoss strata, recording the aggradation and
368 migration of a bar (Fig. 19).

369 Type C compound strata define bar growth at an oblique angle to the net transport
370 direction, and define the lateral migration of a bank-attached bar form (Fig. 10D). The coarser,
371 non-compound type D architectures are interpreted as thalweg deposits (Fig. 15). Together,
372 these four architectural types describe the construction of channel-bottom topography within
373 individual channel belts via the migration and growth of dunes (both on bars and in the
374 thalweg), free bars, and point bars.

375

376 **Channel bed topography**

377 If preserved, bar form topography is interpreted to record the moment of channel
378 abandonment (Fig. 12A to D). Two lines of evidence support this and, significantly, these lines
379 of evidence are true for the Cedar Mountain Formation, as well as nearby outcrop of the
380 Jurassic Morrison Formation, indicating these may be consistent recorders of preserved bar
381 topography (Fig. 12E; location shown in Fig. 1B). First, in both cross section and map view, the
382 compound relationship between dune and bar strata informs us that entire bar forms are
383 preserved, complete with bar rollover (Figs. 12, 13, 14, and 19). Second, the stoss-positioned
384 dune sets are restricted to a surface veneer composing less than the upper 25% of the bar, with
385 the remainder composed of steeply-dipping bar-scale strata. If deflation of ridge surfaces
386 commonly broke through the surface veneer of dune sets, large bar scale strata would
387 constitute a greater percentage of sedimentary structures exposed on ridge surfaces. Instead,
388 dunes occupy approximately an order of magnitude more surface area of the outcrop. The
389 preservation of the river-bottom topography at the time of avulsion is interpreted to be the
390 consequence of a relatively rapid channel abandonment coupled with minimal erosion of the
391 channel-filling deposit by the subsequent channel reoccupation. Additionally, if this paleo-bar
392 topography can be detected using remote sensing, it could be used to better constrain flow
393 depths of ancient rivers from fluvial channel belts exposed at the surface of Mars.

394

395 **Channel planform geometry**

396 The near zero mean values and the high kurtosis of the Cedar Mountain Formation
397 paleo-transport anomaly measurements, coupled with the similarity of the standard deviations

398 measured in the ancient and the modern, are interpreted to indicate that the outcrop geometry
399 preserves the formative river centerline in a reliable way (Fig. 17A to D). Regions of the channel
400 belts showing concentrations of high transport anomaly measurements are associated with
401 point bar lateral accretion surfaces (Figs. 1C, 11, and 16A to B), supporting the hypothesis that
402 lateral point bar migration is a cause of high anomaly measurements (Fig. 4B). However, these
403 regions do not represent a majority of the ridge area.

404 The studied ridges are composed of several vertically-stacked channel-fills. The
405 preservation of the formative river channel centerlines through multiple re-occupations of the
406 channel is expected in fluvial settings with high rates of vertical aggradation within the channel
407 relative to lateral migration rates (Gibling, 2006; Jerolmack and Mohrig, 2007). As a result,
408 there is a general lack of centerline distortion, even though the ridge represents a channel-belt
409 complex. An interesting corollary is that the sinuous planform of the lowest river must have
410 been at least partially inherited from the antecedent surface (e.g., Lazarus and Constantine,
411 2013), as the point bars seem to have been forced by pre-existing curvature rather than driving
412 the formation of channel sinuosity.

413

414 **Channel-belt thickness**

415 Because avulsions are likely to occur when a channel bed has aggraded to a sufficient
416 level of superelevation, the thickness of a preserved channel belt, on average, is posited to
417 equal paleo-channel depth plus an aggradational component. The thickness of a free bar
418 deposit from rollover to bottom is assumed to be a measure of local channel depth (Mohrig et

419 al., 2000). Bar measurements reported in Fig. 8A suggest an overall, mean channel depth of
420 1.28 ± 0.05 m. The mean belt thickness of $3.10 \text{ m} \pm 0.22 \text{ m}$ (Fig. 6C) is then composed of an
421 aggradational component consisting of $1.82 \text{ m} \pm 0.20 \text{ m}$. This indicates that, on average, a
422 channel aggraded to a height of 1.53 ± 0.22 times its original depth before avulsing, creating a
423 channel belt with a total thickness of 2.42 ± 0.19 times its flow depth.

424

425 **Reconstructing river-bed kinematics**

426 *Dune motion on bars and in the thalweg*

427 The theoretical model of Paola and Borgman (1991) demonstrates that in the case of no
428 bed aggradation, bedforms with gamma-distributed heights created cross-sets with thicknesses
429 that follow an exponential distribution. Bridge and Best (1997) and Jerolmack and Mohrig
430 (2005) emphasize the importance of bed aggradation as a control on the distribution of set
431 thickness, showing that increased aggradation rates decrease the relative control of variable
432 scour depth on set thickness. Jerolmack and Mohrig (2005) showed that the coefficient of
433 variation (c_v) of set thicknesses decreases from a value of 0.88 in the case of no aggradation, to
434 values approaching the c_v of the formative bedform heights with significant bed aggradation.
435 Coupled with this change in c_v is a gradual shift from the predicted exponential distribution of
436 set thicknesses, to a gamma distribution mirroring the distribution of the formative bedform
437 heights. Significantly, this analysis has been shown to be general enough to apply to ancient
438 fluvial (Jerolmack and Mohrig, 2005) and aeolian strata (Swanson et al., 2019; Cardenas et al.,
439 2019). Therefore, the reporting and analysis of set thickness distributions should be considered

440 a significant part of any quantitative reconstruction of clastic sedimentary systems where there
441 is an interest in understanding the kinematics and transport within the ancient system.

442 When taken together, all measured dune set thicknesses ($n = 350$) have a c_v of $0.79 \pm$
443 0.04 . While not in the realm of true bypass ($c_v = 0.88 \pm 0.3$; Bridge 1997), the value implies
444 variable scour is the dominant control on stratification. The scour-dominated case also creates
445 laterally discontinuous sets (Jerolmack and Mohrig, 2005; Cardenas et al., 2019). This scour
446 dominance appears to be at odds with the preservation of bar 'form sets' described above (Figs.
447 13 and 14). To understand the construction of the channel belt, measurements must be
448 subdivided by environment and locally normalized. The blind application of these analyses,
449 without considering local architecture, can result in inaccurate interpretations.

450 Set-thickness analysis performed separately for bar lee sets, bar stoss sets, and thalweg
451 sets yields a different result than the bulk average. Set thicknesses were first normalized by
452 their local average value. Normalized cumulative distribution functions (CDFs) are shown in
453 Figure 20. Coefficients of variation for the normalized distributions are 0.29 ± 0.04 for lee sets,
454 0.47 ± 0.07 for stoss sets, and 0.67 ± 0.10 for thalweg sets. Although c_v values as low as 0.29
455 were not examined by Jerolmack and Mohrig (2005), interpolation of their Figure 4B leads to a
456 ratio of aggradation rate to migration rate for lee sets of ~ 0.1 (climb angle from 5 to -6°). Stoss
457 sets have a ratio of $\sim 3.2 \times 10^{-2}$ (climb angle from 1° to 2°), and thalweg sets have a ratio of ~ 3.2
458 $\times 10^{-3}$ (climb angle from 0.1° to 0.2°). The lee sides of downstream-migrating barforms, where
459 the most sediment accumulation is expected (Reesink et al., 2015), have the highest ratio of
460 aggradation rate to migration rate. This significant aggradation is supported by a Kolmogorov-

461 Smirnov statistical test comparing the measurements to fitted exponential and gamma curves
462 (Fig. 20A to C). For lee sets, the exponential curve is rejected at a significance level of 0.05 ($p <$
463 0.001), and the gamma curve is not ($p = 0.46$). This is consistent with the observed stacking and
464 downstream thickening of sets in lee-type architectures (Fig. 14). Even though thalweg sets are
465 rejected as being exponentially distributed ($p = 0.02$) and not rejected as gamma distributed (p
466 $= 0.17$), the two fitted curves are more similar than in the lee and stoss cases.

467 A non-trivial amount of climb is recorded by stoss sets, given the c_v of 0.47 ± 0.07 , and is
468 supported by the rejection of an exponential fit ($p = 0.01$), and non-rejection of a gamma fit ($p =$
469 0.90). This conflicts with the interpretation that these sets are the record of erosive dunes
470 removing sediment from bar stoss slopes and transporting it to bar lee slopes, driving bar
471 migration. The upstream-dipping basal scour surfaces and the presence of few stacked sets
472 support the stoss interpretation (Fig. 13), but a significantly higher c_v of 0.88 ± 0.3 is expected
473 (Paola and Borgman, 1991; Bridge, 1997). Bar stoss slopes are erosional most of the time, as
474 required for bar migration, but by chance, what has been preserved is the record of short-lived
475 episodes of upstream stoss-slope accretion. Using ground-penetrating radar cross sections,
476 Skelly et al. (2003) interpreted upstream accretion in recent fluvial channel-fills of the Niobrara
477 River, Nebraska, USA.

478

479 *Constraints on the time recorded by individual channel belts*

480 How is time distributed through Cedar Mountain channel belts? Backing out
481 sedimentation rates from these strata would provide information on the kinematics of the

482 Cedar Mountain rivers, as well as how local controls might dictate the construction of the rock
 483 record (Sadler, 1981; Jerolmack and Sadler, 2015; Paola et al., 2018). The distribution of cross-
 484 set thicknesses, in conjunction with assumed bedform migration rates, can provide some sense
 485 of how much time is preserved within individual channel belts. Given that the accumulation of
 486 dune sets at the bar lee is the process through which these bars migrated (Fig. 14), it follows
 487 that

$$488 \quad r_{lee} / c_{lee} = s_{bar} / m_{bar} \quad (2)$$

489 where r_{lee} is the aggradation rate of the bed, c_{lee} is the migration rate of dunes, r_{lee} / c_{lee} is
 490 associated with a particular c_v and does not vary significantly with the calculated standard error
 491 (Jerolmack and Mohrig, 2005, their Fig. 4B), and m_{bar} is the dune migration distance required to
 492 stack cross sets up to the average bar thickness, s_{bar} (Fig. 21A-C). Both sides of Equation 2 can
 493 be thought of as equaling the climb angle of a compound barform. Solving for m_{bar} , the only
 494 unknown, yields

$$495 \quad m_{bar} = 1.28 \text{ m} \pm 0.05 \text{ m} / 10^{-1} \quad (3)$$

496 which equals $12.8 \text{ m} \pm 0.5 \text{ m}$ of bar migration. In the North Loup River, downstream-migrating
 497 bars migrate $\sim 10 \text{ m}$ per day (Mohrig and Smith, 1996). Assuming this is a comparable rate to
 498 the ancient Cedar Mountain fluvial system, the observed lee architectures are a record of only
 499 $\sim 1.28 \pm 0.05$ days of sedimentation. This suggests the bar strata and associated compound dune
 500 strata do not record the gradual aggradation of the channel bed leading up to avulsion, but
 501 rather record the higher frequency modification of the channel bed via bar migration. Instead,
 502 it is hypothesized that the gradual aggradation of the channel bed is recorded in thalweg strata.

503 To test this hypothesis, Equation 2 is redefined in terms of the thalweg sets and the average
504 channel belt thickness:

$$505 \quad r_{thalweg} / C_{thalweg} = S_{belt} / m_{thalweg} \quad (4)$$

506 Solving for the amount of necessary dune migration to construct the thalweg component of the
507 mean channel belt thickness,

$$508 \quad m_{thalweg} = 1.82 \text{ m} \pm 0.20 \text{ m} / 10^{-2.5} \quad (5)$$

509 which equals 576 m \pm 63 m of necessary dune migration (Fig. 21A-C). The average
510 instantaneous dune migration rate in the North Loup, independent of flow size or dune depth,
511 is 60 m per day (Mohrig and Smith, 1996). Although dune migration rates have not been
512 reconstructed in the ancient Cedar Mountain rivers, the North Loup is at least a sand-bed river
513 with interacting dunes and bars (Mohrig and Smith, 1996), and should provide a reasonable
514 order of magnitude estimation. Assuming steady construction at this rate, only 9.7 days \pm 1.1
515 days are required to accumulate the thalweg strata reported here. This rejects the hypothesis
516 that the thalweg strata record the gradual aggradation of the channel bed over its total
517 occupation. For most rivers, occupation may last anywhere from years to thousands of years
518 (Stouthamer and Berendsen, 2001; Slingerland and Smith, 2004). It is unlikely these channels
519 were only occupied for 9.7 days. Instead, these strata may only represent the aggradation that
520 occurred during the final episode of sedimentation that preceded avulsion and channel
521 abandonment. This episode is likely to coincide with the final flood prior to avulsion.

522 This result suggests that the channel was instead in a state of bypass for most of its
523 occupation. Had channel abandonment not prevented it, the aggradation recorded by each
524 channel belt would likely have been completely reworked. The complete reworking of the
525 channel bed has, in fact, been observed in modern net-depositional rivers (Nittrouer et al.,
526 2011a). This also suggests that floodplain deposits might more completely record successive
527 episodes of flood-stage deposition than channel fills, as presumably an episode of floodplain
528 deposition is not immediately followed by reworking and removal.

529 Alternatively, the aggradation of the thalweg may represent $9.7 \text{ days} \pm 1.1 \text{ days}$ of
530 accumulation spread intermittently over a longer time period, as much as $335 \text{ days} \pm 55 \text{ days}$ if
531 a commonly assumed intermittency, the fraction of time per year spent at bankfull flow, of 0.02
532 is used (Parker et al., 1998). However, there is no stratigraphic indicator that the accumulations
533 within a single channel belt are the product of multiple small depositional episodes separated
534 by hiatuses (e.g., aeolian reworking, Carling and Leclair, 2019). Accounting for this would
535 require the assumptions that there was no reworking of the channel bed between depositional
536 episodes (e.g., significant channel bed reworking shown in Nittrouer et al., 2011b; Shaw and
537 Mohrig, 2014; Mason and Mohrig, in review), and that dune migration perfectly resumed right
538 where the previous episode of sedimentation left off. It is more likely that such gradual bed
539 aggradation would produce a scour-and-fill style architecture and a higher c_v of 0.88 ± 0.03
540 (e.g., Paola and Borgman, 1991; Bridge and Best, 1997; Bridge, 1997; Jerolmack and Mohrig,
541 2005; Cardenas et al., 2019). This is not to say that an intermittency of 0.02 is impossible or
542 unlikely for these rivers; it simply cannot be constrained using only the accumulation rates of
543 the final episode of sedimentation along a continuously reworked channel bed.

544

545 **Channel vs. floodplain accumulation**

546 On average, a Cedar Mountain river constructed a channel belt of thickness 2.42 ± 0.19
547 times its original depth before avulsing, based on the ratio of channel-belt thickness to flow
548 depth. This is a slightly higher value than reported for the Guadalupe-Matarranya ancient fluvial
549 system in Spain (Mohrig et al., 2000). Mohrig et al. (2000) report an average superelevation of
550 0.61 times flow depth before avulsion occurs from the Guadalupe-Matarranya ancient fluvial
551 system in Spain. In their Table 2, the sum of the incision depth and superelevation is equal to
552 the belt thickness measurements presented here. Dividing their belt thickness measurements
553 by local channel depth yields a smaller amount of average total aggradation before avulsion of
554 1.84 times channel depth. This suggests the ancient Cedar Mountain fluvial system was able to
555 support more channel bed aggradation before avulsing, suggesting a higher ratio of floodplain
556 aggradation rate to channel bed aggradation rate than in the Guadalupe-Matarranya system
557 (Mohrig, 2000). This is consistent with the punctuated style of channel-bed aggradation
558 interpreted from the time needed to accumulate the thalweg deposits. In this scenario, most of
559 the sediment rapidly accumulated in the channel during a bankfull episode is reworked to zero
560 net accumulation shortly after. This is coupled with a contrasting steady, gradual levee and
561 floodplain aggradation, assuming these overbank environments are less likely to be reworked
562 to a state of zero net aggradation between floods. That is, in order for the channel bed to reach
563 the threshold superelevation to avulse, more channel bed aggradation was required during the
564 final depositional episode to catch up with steadily aggraded levees and floodplain (Fig. 22).

565

566 **Comparison to other fluvial systems and strata**

567 The Cedar Mountain rivers may represent an end-member behavior, opposite to a
568 channel bed undergoing steady aggradation and frequent but partial reworking, such as
569 described in Carling and Leclair (2019). In that work, an entrenched reach of the Luni River,
570 India, is shown to repeatedly partially rework and scour its bed during floods, but optically-
571 stimulated luminescence age dates show a trend of increasing age with depth, topping out at
572 1.9 ka (their Table 2). This is a record of slow, steady bed aggradation over the last 1.9 ka with
573 each flood, rather than the rapid sedimentation frozen in place following channel abandonment
574 in the Cedar Mountain. As another counter example, the Cretaceous McMurray Formation,
575 seismically imaged in the subsurface of Alberta, Canada, has recorded multiple channel widths
576 of lateral accretion and meander bend cutoffs within the channel belt, which has been
577 demonstrated to drive the erosion of formative channel elements (Durkin et al., 2018), as well
578 as alter the geometry of the channel belt relative to the formative river channel (their Fig. 12).
579 Durkin et al. (2018) estimate a minimum of 4,000 years to produce the observed reworking.
580 Indeed, heavily reworked examples of fluvial strata exist, and the given examples require
581 contrasting processes to the Cedar Mountain ancient fluvial system. Their accumulations
582 represent longer time scales, as well. River avulsions into local topographic lows formed
583 between abandoned, raised channel beds has been shown to locally increase sedimentation
584 rates and prevent reworking, leading to well-preserved channel belts at the km scale (Swartz et

585 al., in prep; Cardenas et al., in prep). Given the total extent of the Cedar Mountain ridges and
586 the relatively rapid sedimentation rates, this process may also be at work here.

587

588 **CONCLUSIONS**

589 The belts of the Cedar Mountain Formation represent rivers that avulsed frequently
590 enough to limit lateral migration of any single channel. This is similar to the kinematics of
591 megafan channels, which can avulse on the scale of years and don't generally migrate to any
592 significant degree (e.g., Horton and DeCelles, 2001; Chakraborty et al., 2010), although the time
593 required to aggrade the thalwegs required an environment capable of sustaining sediment-
594 transporting flows for at least 9 days continuously. In addition to capturing what may be a
595 common bankfull event, 41% of any belt represents a day's worth of free bar migration. This
596 further supports the 'strange ordinariness' (Paola et al., 2018) of much of the stratigraphic
597 record, as well as the frequently observed phenomenon that most of the time represented in a
598 stratigraphic section is recorded by erosional or hiatal surfaces between punctuated
599 depositional episodes, rather than the accumulations (Sadler, 1981; Miall, 2015; Sadler and
600 Jerolmack, 2015; Paola et al., 2018). This methodology provides a framework for the
601 quantitative analysis of other modern and ancient fluvial systems. The distribution of dune
602 cross-set thicknesses within the context of bar topography is the dataset at the root of this
603 analysis, and should be emphasized in future field campaigns, including the exhumed fluvial
604 strata that will be examined during the 2020 Mars rover mission to Jezero crater (Goudge et al.,
605 2018).

606

607 **ACKNOWLEDGEMENTS**

608 Hima Hassenruck-Gudipati, Woong Mo Koo, and David Brown are thanked for their field
609 assistance. The staff of Green River State Park, Utah, were accommodating to our large group.
610 This work has improved following discussions with members of the David Mohrig Research
611 Group and the Quantitative Clastics Laboratory, as well as Paola Passalacqua, Alistair Hayden,
612 Mike Lamb, Jenn Pickering, and Tim Demko. Funding was provided by the University of Texas
613 Jackson School of Geosciences, the University of Texas Graduate School, and the RioMAR
614 Industry Consortium.

615

616 **DATA AVAILABILITY**

617 The data that support the findings of this study are available from the corresponding
618 author upon reasonable request.

619

620 **REFERENCES**

621 **Allen, J.R.L.** (1970) A Quantitative Model of Climbing Ripples and Their Cross-Laminated Deposits.
622 *Sedimentology*, **14**, 5–26.

- 623 **Allen, J.R.L.** (1983) Studies in fluvial sedimentation: bars, bar-complexes and sandstone sheets (low-
624 sinuosity braided streams) in the Brownstones (L. Devonian), Welsh Borders. *Sedimentary*
625 *Geology*, **33**, 237–293.
- 626 **Almeida, R.P., Freitas, B.T., Turra, B.B., Figueiredo, F.T., Marconato, A., and Janikian, L.** (2016)
627 Reconstructing fluvial bar surfaces from compound cross-strata and the interpretation of bar
628 accretion direction in large river deposits. *Sedimentology*, **63**, 609–628.
- 629 **Berens, P.** (2009) CircStat: A MATLAB Toolbox for Circular Statistics. *Journal of Statistical Software*, **31**, 1-
630 21.
- 631 **Bridge, J.S.** (1997) Thickness of sets of cross strata and planar strata as a function of formative bed-wave
632 geometry and migration, and aggradation rate. *Geology*, **25**, 971-974.
- 633 **Bridge, J.S., and Best, J. (1997)** Preservation of planar laminae due to migration of low-relief bed waves
634 over aggrading upper-stage plane beds: comparison of experimental data with theory.
635 *Sedimentology*, **44**, 253-262.
- 636 **Burr, D.M., Enga, M.-T., Williams, R.M., Zimbelman, J.R., Howard, A.D., and Brennand, T.A.** (2009)
637 Pervasive aqueous paleoflow features in the Aeolis/Zephyria Plana region, Mars. *Icarus*, **200**, 52-
638 76.
- 639 **Cardenas, B.T., Mohrig, D., and Goudge, T.A.** (2018) Fluvial stratigraphy of valley fills at Aeolis Dorsa,
640 Mars: Evidence for base-level fluctuations controlled by a downstream water body. *Geological*
641 *Society of America Bulletin*, **130**, 484-498.
- 642 **Cardenas, B.T., Kocurek, G., Mohrig, D., Swanson, T., Hughes, C.M., and Brothers, S.C.** (accepted)
643 Preservation of autogenic processes and allogenic forcings within set-scale aeolian architecture

- 644 II: the scour-and-fill dominated Jurassic Page Sandstone, Arizona, USA. *Journal of Sedimentary*
645 *Research*.
- 646 **Cardenas, B.T., Swartz, J.M., Mohrig, D., Prokocki, E.W.** Setting up the preservation of fluvial channel
647 belts. *Geology*, in review.
- 648 **Carling, P.A., and Leclair, S.F.** (2019) Alluvial stratification styles in a large, flash-flood influenced dryland
649 river: The Luni River, Thar Desert, north-west India. *Sedimentology*, **66**, 102-128.
- 650 **Chakraborty, T., Kar, R., Ghosh, P., and Basu, S.** (2010) Kosi megafan: Historical records, geomorphology
651 and the recent avulsion of the Kosi River. *Quaternary International*, **227**, 143-160.
- 652 **Chamberlin, E.P., and Hajek, E.A.** (2015) Interpreting paleo-avulsion dynamics from multistory sand
653 bodies. *Journal of Sedimentary Research*, **85**, 82–94.
- 654 **Chamberlin, E.P., and Hajek, E.A.** (2019) Using bar preservation to constrain reworking in channel-
655 dominated fluvial stratigraphy. *Geology*, **47**, 531-534.
- 656 **Cuevas Martínez, J.L., Cabrera Pérez, L., Marcuello, A., Arbués Cazo, P., Marzo Carpio, M., and**
657 **Bellmunt, F.** (2010) Exhumed channel sandstone networks within fluvial fan deposits from the
658 Oligo-Miocene Caspe Formation, South-east Ebro Basin (North-east Spain). *Sedimentology*, **57**,
659 162–189.
- 660 **Currie, B.S.** (1998) Upper Jurassic-Lower Cretaceous Morrison and Cedar Mountain Formations, Ne
661 Utah-NW Colorado: Relationships between Nonmarine Deposition and Early Cordilleran
662 Foreland-Basin Development. *Journal of Sedimentary Research*, **68**, 632-652.
- 663 **Davis, J.M., Balme, M., Grindrod, P.M., Williams, R.M.E., and Gupta, S.** (2016) Extensive Noachian
664 fluvial systems in Arabia Terra: implications for early Martian climate. *Geology*, **44**, 847-850.

- 665 **DeCelles, P.G., Langford, R.P., and Schwartz, R.K.** (1983) Two New Methods of Paleocurrent
666 Determination from Trough Cross-Stratification. *Journal of Sedimentary Research*, **53**, 629-642.
- 667 **Dietrich, W.E., and Smith, J.D.** (1984) Bed load transport in a river meander. *Water Resources Research*,
668 **20**, 1355-1380.
- 669 **Dott, R.H., Jr.** (1973) Paleocurrent Analysis of Trough Cross Stratification. *Journal of Sedimentary*
670 *Research*, **43**, 779-783.
- 671 **Durkin, P.R., Hubbard, S.M., Holbrook, J., and Boyd, R.** (2018) Evolution of fluvial meander-belt
672 deposits and implications for the completeness of the stratigraphic record. *Geological Society of*
673 *America Bulletin*, **130**, 721-739.
- 674 **Edmonds, D.A., Hajek, E.A., Downton, N., and Bryk, A.B.** (2016) Avulsion flow-path selection on rivers in
675 foreland basins. *Geology*, **44**, 695–698.
- 676 **Edwards, M.B., Eriksson, K.A., and Kier, R.S.** (1983) Paleochannel geometry and flow patterns
677 determined from exhumed Permian point bars in north-central Texas. *Journal of Sedimentary*
678 *Research*, **53**, 1261-1270.
- 679 **Friend, P.F., Slater, M.J., and Williams, R.C.** (1979) Vertical and lateral building of river sandstone
680 bodies, Ebro Basin, Spain. *Journal of the Geological Society*, **136**, 39–46.
- 681 **Ganti, V., Paola, C., and Fofoula-Georgiou, E.** (2013) Kinematic controls on the geometry of the
682 preserved cross sets. *Journal of Geophysical Research: Earth Surface*, **118**, 1296-1307.
- 683 **Garrison, J.R., Brinkman, D., Nichols, D.J., Layer, P., Burge, D., and Thayn, D.** (2007) A multidisciplinary
684 study of the Lower Cretaceous Cedar Mountain Formation, Mussentuchit Wash, Utah: a

685 determination of the paleoenvironment and paleoecology of the Eolambia caroljonesa dinosaur
686 quarry. *Cretaceous Research*, **28**, 461–494.

687 **Gibling, M.R.** (2006) Width and thickness of fluvial channel bodies and valley fills in the geological
688 record: a literature compilation and classification. *Journal of Sedimentary Research*, **76**, 731–
689 770.

690 **Goudge, T.A., Mohrig, D., Cardenas, B.T., Hughes, C.M., and Fassett, C.I.** (2018) Stratigraphy and
691 paleohydrology of delta channel deposits, Jezero crater, Mars. *Icarus*, **301**, 58–75.

692 **Hajek, E.A., and Edmonds, D.A.** (2014) Is river avulsion style controlled by floodplain morphodynamics?
693 *Geology*, **42**, 199-202.

694 **Hayden, A.T., Lamb, M.P., Fischer, W.W., Ewing, R.C., McElroy, B.J., and Williams, R.M.E.** (2019)
695 Formation of sinuous ridges by inversion of river-channel belts in Utah, USA, with implications
696 for Mars. *Icarus*, **332**, 91-110.

697 **Heller, P.L., and Paola, C.** (1996) Downstream changes in alluvial architecture: an exploration of controls
698 on channel-stacking patterns. *Journal of Sedimentary Research*, **66**, 297-306.

699 **Hooke, J.M., and Yorke, L.** (2011) Channel bar dynamics on multi-decadal timescales in an active
700 meandering bar. *Earth Surface Processes and Landforms*, **36**, 1910-1928.

701 **Hughes, C.M., Cardenas, B.T., Goudge, T.A., and Mohrig, D.** (2019) Deltaic deposits indicative of a
702 paleo-coastline at Aeolis Dorsa, Mars. *Icarus*, **317**, 442-453.

703 **Ikeda, H.** (1989) Sedimentary controls on channel migration and origin of point bars in sand-bedded
704 meandering rivers. In S. Ikeda and G. Parker (Eds.), *River Meandering: Water Resources*
705 *Monograph*, **12**, 51-68. American Geophysical Union: Washington, D.C.

- 706 **Ikeda, S., Parker, G., and Sawai, K.** (1981) Bend theory of river meanders. Part 1. Linear development.
707 *Journal of Fluid Mechanics*, **112**, 363-377.
- 708 **Jerolmack, D.J., and Mohrig, D.** (2005) Frozen dynamics of migrating bedforms. *Geology*, **33**, 57-60.
- 709 **Jerolmack, D.J., and Mohrig, D.** (2007) Conditions for branching in depositional rivers. *Geology*, **35**, 463–
710 466.
- 711 **Jones, H.L., and Hajek, E.A.** (2007) Characterizing avulsion stratigraphy in ancient alluvial deposits.
712 *Sedimentary Geology*, **202**, 124-137.
- 713 **Kowallis, B.J., Heaton, J.S., and Bringhurst, K.** (1986) Fission-track dating of volcanically derived
714 sedimentary rocks. *Geology*, **14**, 19-22.
- 715 **Lazarus, E.D., and Constantine, J.A.** (2013) Generic theory for channel sinuosity. *Proceedings of the*
716 *National Academy of Sciences*, **110**, 8447-8452.
- 717 **Mahon, R.C., and McElroy, B.** (2018) Indirect estimation of bedload flux from modern sand-bed rivers
718 and ancient fluvial strata. *Geology*, **46**, 579-582.
- 719 **Maizels, J.K.** (1987) Plio-Pleistocene raised channel systems of the western Sharqiya (Wahiba), Oman.
720 *Geological Society of London, Special Publications*, **35**, 31–50.
- 721 **Maizels, J.** (1990) Raised channel systems as indicators of palaeohydrologic change: a case study from
722 Oman. *Palaeogeography, Palaeoclimatology, Palaeoecology*, **76**, 241–277.
- 723 **Maizels, J., and McBean, C.** (1990) Cenozoic alluvial fan systems of interior Oman: palaeoenvironmental
724 reconstruction based on discrimination of palaeochannels using remotely sensed data.
725 *Geological Society of London, Special Publications*, **49**, 565–582.

- 726 **Mason, J., and Mohrig, D.** (2018) Using time-lapse lidar to quantify river bend evolution on the
727 meandering coastal Trinity River, Texas, USA. *Journal of Geophysical Research: Earth Surface*,
728 **123**, 1133-1144.
- 729 **Mason, J., and Mohrig, D.** (submitted) Scroll bars are inner bank levees along bends in meandering
730 rivers.
- 731 **Mason, J., and Mohrig, D.** (submitted?) Bedform group stuff introducing sonar dataset
- 732 **McKee, E.D., and Weir, G.W.** (1953) Terminology for stratification and cross-stratification in
733 sedimentary rocks. *Geological Society of America Bulletin*, **64**, 381–390.
- 734 **Miall, A.D.** (1977) A review of the braided-river depositional environment. *Earth-Science Reviews*, **13**, 1-
735 62.
- 736 **Miall, A.D.** (1985) Architectural-element analysis: a new method of facies analysis applied to fluvial
737 deposits. *SEPM Special Publication–Recognition of Fluvial Depositional Systems and Their*
738 *Resource Potential*, **19**, 33-81.
- 739 **Miall, A.D.** (1988) Architectural elements and bounding surfaces in fluvial deposits: anatomy of the
740 Kayenta formation (lower Jurassic), Southwest Colorado. *Sedimentary Geology*, **55**, 233–262.
- 741 **Miall, A.D.** (2015) Updating uniformitarianism: stratigraphy as just a set of ‘frozen accidents’. *Geological*
742 *Society of London, Special Publications*, **404**, 11-36.
- 743 **Mohrig, D., Heller, P.L., Paola, C., and Lyons, W.J.** (2000) Interpreting avulsion process from ancient
744 alluvial sequences: Guadalupe-Matarranya system (northern Spain) and Wasatch Formation
745 (western Colorado). *Geological Society of America Bulletin*, **112**, 1787–1803.

- 746 **Mohrig, D., and Smith, J.D.** (1996) Predicting the migration rates of subaqueous dunes. *Water Resources*
747 *Research*, **32**, 3207-3217.
- 748 **Nittrouer, J.A., Mohrig, D., Allison, M.A., and Peyret, A.-P. B.** (2011a) The lowermost Mississippi River:
749 a mixed bedrock-alluvial channel. *Sedimentology*, **58**, 1914-1934.
- 750 **Nittrouer, J.A., Mohrig, D., and Allison, M.** (2011b) Punctuated sand transport in the lowermost
751 Mississippi River. *Journal of Geophysical Research: Earth Surface*, **116**, F04025.
- 752 **Nuse, B.** (2015) Flow processes and sedimentation in a low-sinuosity high net-sand content fluvial
753 channel belt: 3D outcrop study of the Cedar Mountain Formation, Utah. *Unpublished MS Thesis*,
754 *Colorado School of Mines*.
- 755 **Paola, C., and Borgman, L.** (1991) Reconstructing random topography from preserved stratification.
756 *Sedimentology*, **38**, 553-565.
- 757 **Paola, C., Ganti, V., Mohrig, D., Runkel, A.C., and Straub, K.M.** (2018) Time not our Time: Physical
758 controls on the preservation and measurement of geologic time. *Annual Review of Earth and*
759 *Planetary Sciences*, **46**, 409-438.
- 760 **Parker, G., Paola, C., Whipple, K.X., and Mohrig, D.** (1998) Alluvial fans formed by channelized fluvial
761 and sheet flow. I: Theory: *Journal of Hydraulic Engineering*, **124**, 985-995.
- 762 **Parker, G., Wilcock, P.R., Paola, C., Dietrich, W.E., and Pitlick, J.** (2007) Physical basis for quasi-universal
763 relations describing bankfull hydraulic geometry of single-thread gravel bed rivers. *Journal of*
764 *Geophysical Research – Earth Surface*, **112**, F04005.
- 765 **Peterson, F., and Ryder, R.T.** (1975) Cretaceous rocks in the Henry Mountains region, Utah and their
766 relation to neighboring regions. in *Four Corners Geological Society Guidebook*, **8**, p. 166-189.

- 767 **Pizzuto, J.E.** (1987) Sediment diffusion during overbank flows. *Sedimentology*, **34**, 301–317.
- 768 **Reesink, A.J.H., Van den Berg, J.H., Parsons, D.R., Amsler, M.L., Best, J.L., Hardy, R.J., Orfeo, O., and**
769 **Szupiany, R.N.** (2015) Extremes in dune preservation: Controls on the completeness of fluvial
770 deposits. *Earth-Science Reviews*, **150**, 652-665.
- 771 **Reitz, M.D., Jerolmack, D.J., and Swenson, J.B.** (2010) Flooding and flow path selection on alluvial fans
772 and deltas. *Geophysical Research Letters*, **37**, L06401.
- 773 **Rubin, D.M.** (1987) Cross-bedding, Bedforms, and Paleocurrents. *SEPM Concepts in Sedimentology and*
774 *Paleontology*, **1**.
- 775 **Rubin, D.M., and Hunter, R.E.** (1982) Bedform climbing in theory and nature. *Sedimentology*, **29**, 121–
776 138.
- 777 **Rubin, D.M., and Hunter, R.E.** (1987) Bedform alignment in directionally varying flows. *Science*, **237**,
778 276-278.
- 779 **Sadler, P.M.** (1981) Sediment accumulation rates and the completeness of stratigraphic sections. *The*
780 *Journal of Geology*, v. 89, 569-584.
- 781 **Sadler, P.M., and Jerolmack, D.J.** (2015) Scaling laws for aggradation, denudation and progradation
782 rates: the case for time-scale invariance at sediment sources and sinks. *Geological Society of*
783 *London, Special Publications*, **404**, 69-88.
- 784 **Seminara, G., and Tubino, M.** (1989) Alternate bars and meandering: Free, forced and mixed
785 interactions. In S. Ikeda and G. Parker (Eds.), *River Meandering: Water Resources Monograph*,
786 **12**, 267-320. American Geophysical Union: Washington, D.C.

- 787 **Shaw, J.B., and Mohrig, D.** (2014) The importance of erosion in distributary channel network growth,
788 Wax Lake Delta, Louisiana, USA: *Geology*, **42**, 31-34.
- 789 **Skelly, R.L., Bristow, C.S., and Ethridge, F.G.** (2003) Architecture of channel-belt deposits in an
790 aggrading shallow sandbed braided river: the lower Niobrara River, northeast Nebraska.
791 *Sedimentary Geology*, **158**, 249-270.
- 792 **Slingerland, R., and Smith, N.D.** (2004) River avulsions and their deposits. *Annual Review of Earth and*
793 *Planetary Sciences*, **32**, 257-285.
- 794 **Stokes, W.L.** (1961) Fluvial and Eolian Sandstone Bodies in Colorado Plateau. *AAPG SP-Geometry of*
795 *Sandstone Bodies*, **22**, 151-178.
- 796 **Stouthamer, E., and Berendsen, H.J.A.** (2001) Avulsion frequency, avulsion duration, and interavulsion
797 period of Holocene channel belts in the Rhine-Meuse Delta, the Netherlands. *Journal of*
798 *Sedimentary Research*, **71**, 589-598.
- 799 **Swanson, T., Mohrig, D., Kocurek, G., Perillo, M., and Venditti, J.** (2018) Bedform spurs: a result of a
800 trailing helical vortex wake. *Sedimentology*, **65**, 191-208.
- 801 **Swanson, T., Mohrig, D., Kocurek, G., Cardenas, B.T., and Wolinsky, M.A.** (2019) Preservation of
802 autogenic processes and allogenic forcings within set-scale aeolian architecture I: numerical
803 experiments. *Journal of Sedimentary Research*.
- 804 **Swartz, J.M., Mohrig, D., Passalacqua, P., Goff, J., and Gulick, S.P.S.** (2018) From distributary to
805 tributary: coastal drainage network position and morphometry are set by depositional
806 processes. *Presented at the American Geophysical Union 2018 Fall Meeting*, EP21B-2230.

- 807 **Van De Lagewag, W.Y., Van Dijk, W.M., and Kleinhans, M.G.** (2013) Channel belt architecture formed
808 by a meandering river. *Sedimentology*, **60**, 840-859.
- 809 **Wang, J., and Bhattacharya, J.P.** (2017) Plan-view paleochannel reconstruction of amalgamated
810 meander belts, Cretaceous Ferron Sandstone, Notom Delta, south-central Utah, U.S.A. *Journal*
811 *of Sedimentary Research*, **88**, 58–74.
- 812 **Whiting, P.J., and Dietrich, W.E.** (1993) Experimental constraints on bar migration through bends:
813 Implications for meander wavelength selection. *Water Resources Research*, **29**, 1091-1102.
- 814 **Williams, R.M.E., Irwin, R.P., and Zimelman, J.R.** (2009) Evaluation of paleohydrologic models for
815 terrestrial inverted channels: Implications for application to Martian sinuous ridges.
816 *Geomorphology*, **107**, 300–315.
- 817 **Williams, R.M.E., Chidsey Jr., T.C., and Eby, D.E.** (2007) Exhumed Paleochannels in Central Utah—
818 Analogs for Raised Curvilinear Features on Mars. *Central Utah-Diverse Geology of a Dynamic*
819 *Landscape*, 221–235.
- 820 **Wright, S., and Parker, G.** (2003) Grain-size specific suspended sediment transport and flow resistance
821 in large sand-bed rivers. In A. Gyr and W. Kinzelbach (Eds.), *Sedimentation and Sediment*
822 *transport*, 221-227. Netherlands: Springer.
- 823 **Wu, C., Bhattacharya, J.P., and Ullah, M.S.,** (2015) Paleohydrology and 3D facies architecture of ancient
824 point bars, Ferron Sandstone, Notom Delta, South-central Utah, USA. *Journal of Sedimentary*
825 *Research*, **85**, 399–418.

- 826 **Wu, C., Ullah, M.S., Lu, J., and Bhattacharya, J.P.** (2016) Formation of point bars through rising and
827 falling flood stages: Evidence from bar morphology, sediment transport and bed shear stress.
828 *Sedimentology*, **63**, 1458–1473.
- 829 **Zaki, A.S., Pain, C.F., Edgett, K.S., and Giegengack, R.** (2018) Inverted stream channels in the Western
830 Desert of Egypt. Synergistic remote, field observations and laboratory analysis on Earth with
831 applications to Mars. *Icarus*, **309**, 105-124.

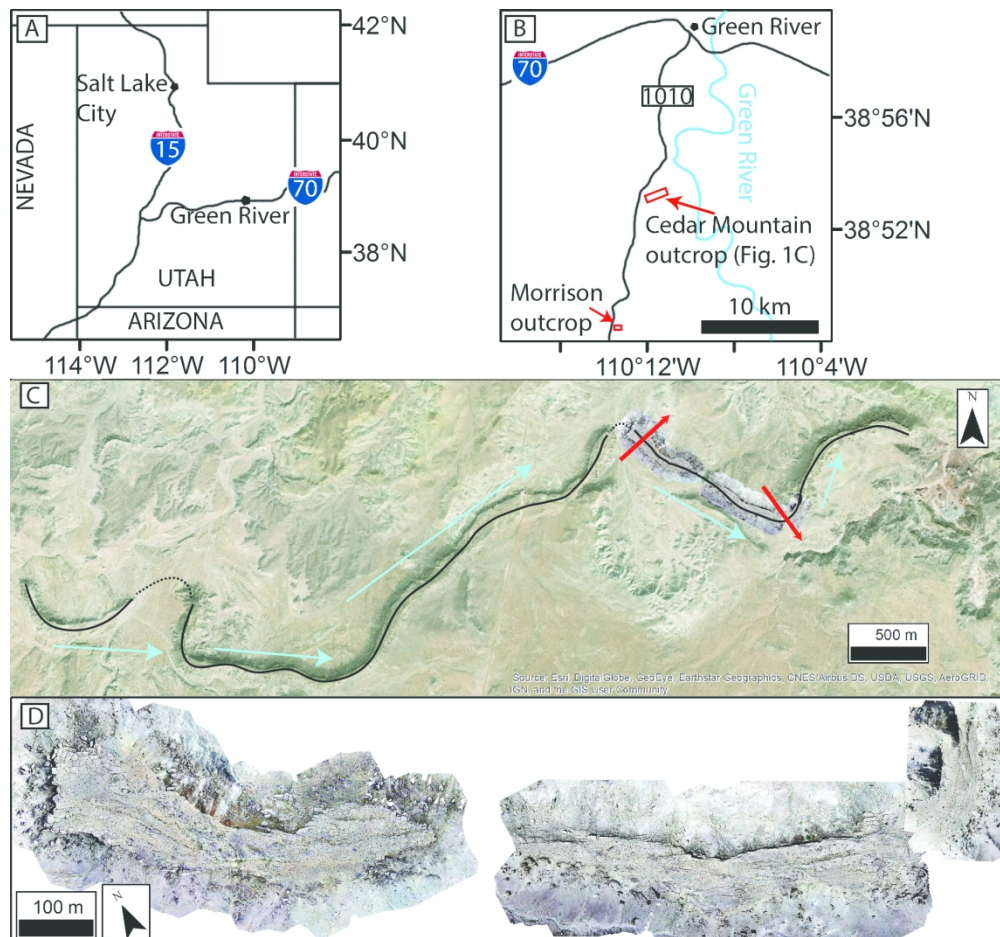


Figure 1 - (A) Map of Utah showing major highways, Salt Lake City and Green River. (B) Zoom in near Green River, showing the location of the town as well as the studied ridges of the Cedar Mountain and the Morrison Formation south of town along 1010. (C) Zoomed out view showing the Cedar Mountain ridges beyond the study area. Black line maps out a ridge centerline for several km, with interpreted dashed segments bridging erosional discontinuities. Teal arrows show the general direction of paleoflow. Red arrows mark the two major bends bounding the studied part of the ridge. The arrows point away from the center of curvature, and match with the general dip directions of local dipping bar strata. (D) Drone ortho-images of the studied eastern and western ridges of the Cedar Mountain Formation ridges. The photomosaics are rotated slightly to fit the panel, but are correctly co-located.

170x157mm (300 x 300 DPI)

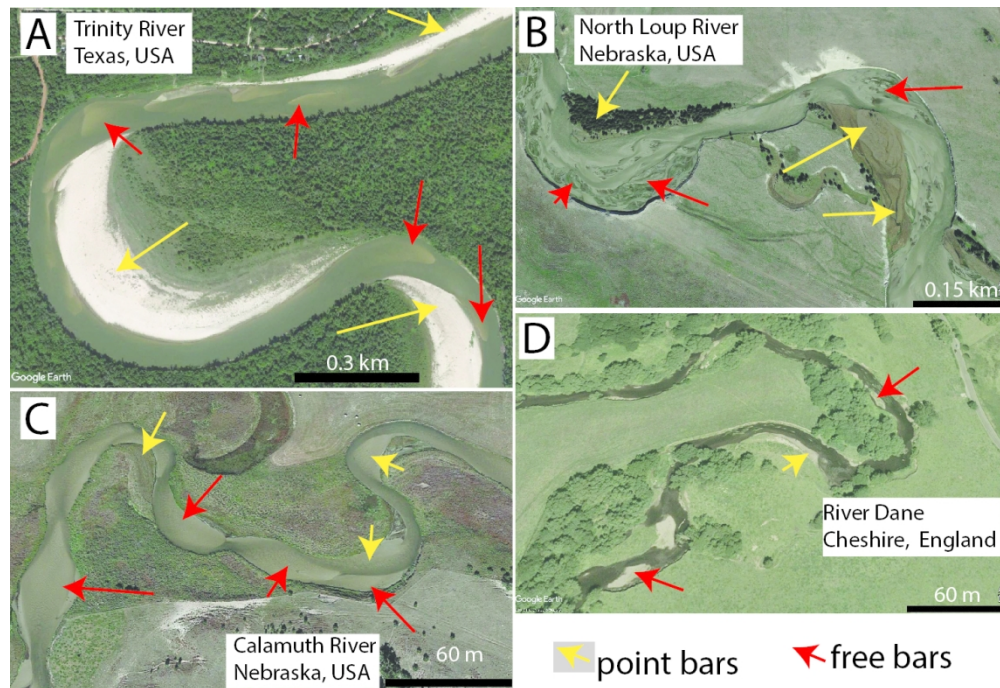


Figure 2 – Free bars (red arrows) and point bars (yellow arrows) commonly coexist in rivers, both in straight reaches and bends. (A) Trinity River, Texas, USA. Image centered at 30.134° N, -94.815° E. (B) North Loup River, Nebraska, USA. Image centered at 42.019° N, -100.098° E. (C) Calamuth River, Nebraska, USA. Image centered at 42.083° N, -99.649° E. (D) River Dane, Cheshire, England. Image centered at 53.183° N, -2.259° E.

124x85mm (300 x 300 DPI)

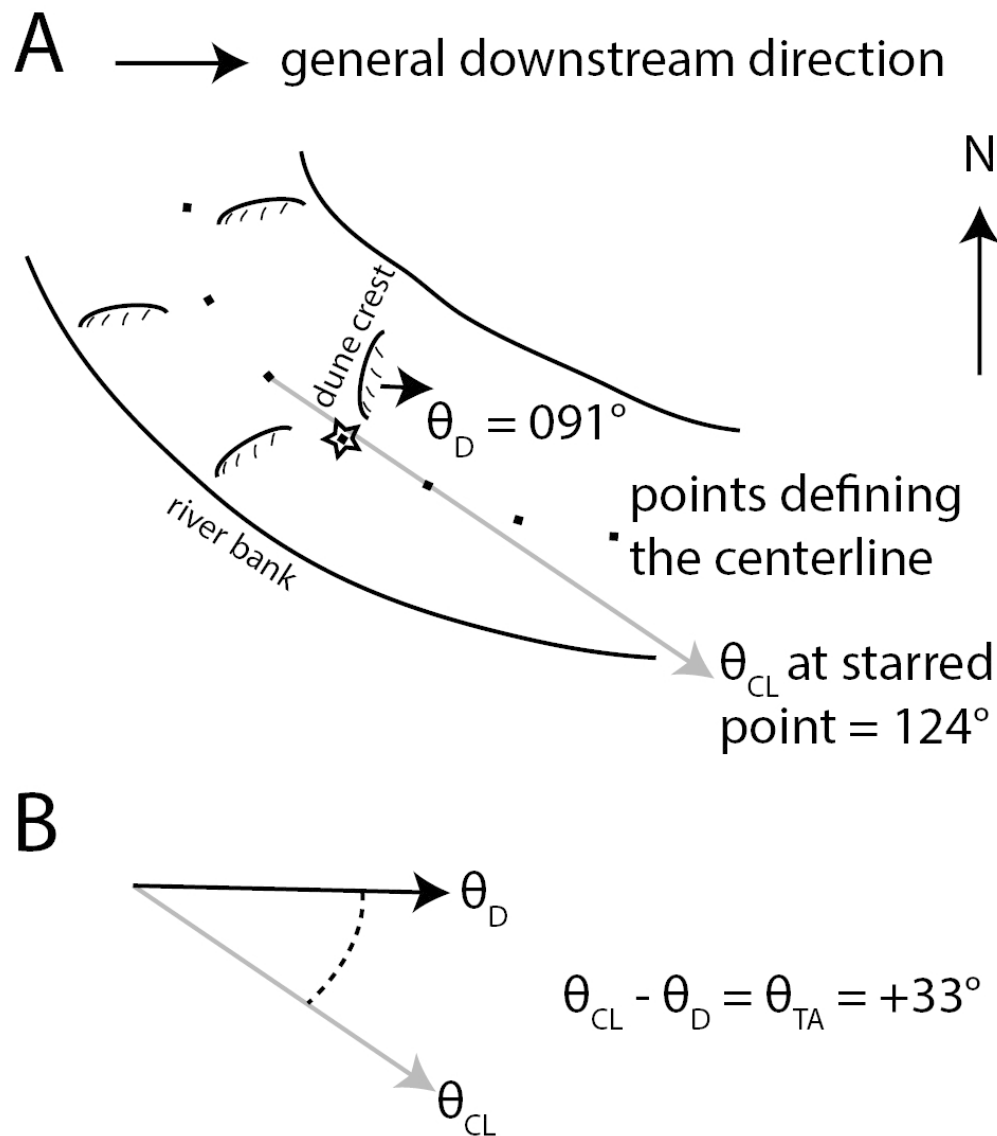


Figure 3 – (A) Diagram defining the components of the transport anomaly, θ_{TA} , for a modern river channel. A measurement of transport direction, θ_D , is made from the orientation of a dune crest (short black arrow; 091°). The centerline point closest to the measurement of θ_D is starred. The orientation of the starred centerline point, θ_{CL} , is defined as the trend of the ray originating at the adjacent upstream point and passing through the adjacent downstream point (gray arrow; 124°). (B) The transport anomaly, θ_{TA} , is defined as $\theta_{CL} - \theta_D$. It may be positive or negative, and is bound between -180° and positive 180° . In this scenario, $\theta_{TA} = 124^\circ - 091^\circ = 33^\circ$.

80x91mm (300 x 300 DPI)

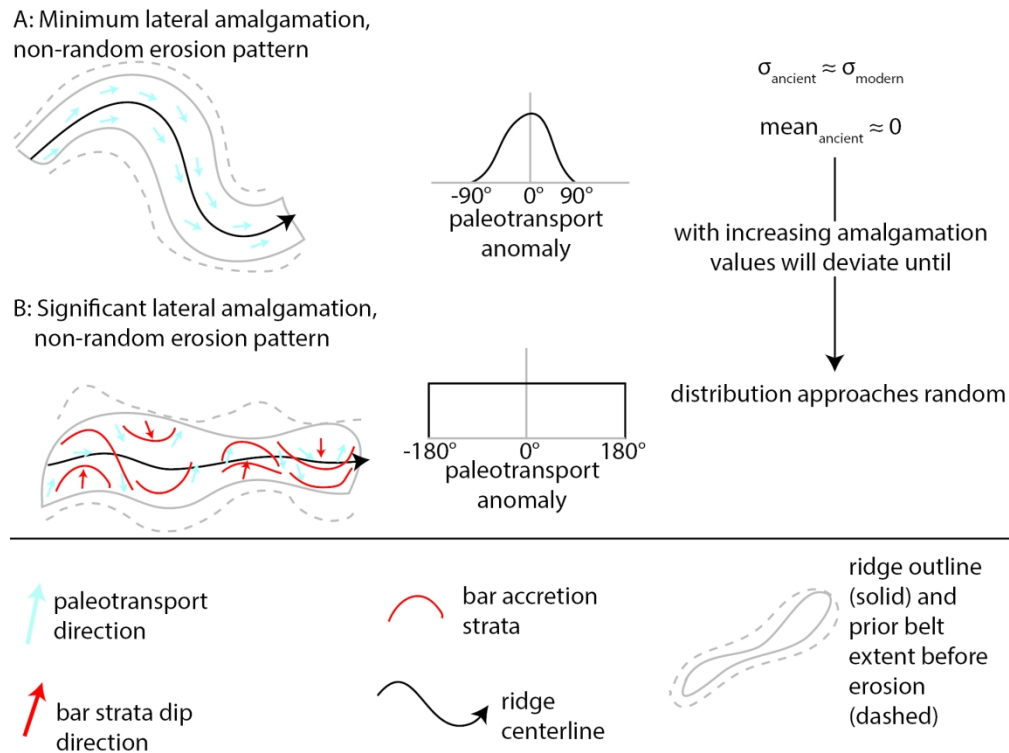


Figure 4 – Hypothesized scenarios guiding interpretations of paleotransport anomaly results. Schematic diagrams are on the left, the distribution of paleotransport anomaly measurements are in the middle, and relevant statistical moments are on the right. Standard deviation is shown by σ . Legend is at the bottom.

(A) The ridge centerline represents well the formative channel centerline. With increasing lateral amalgamation, results will instead approach the scenario in panel B. (B) Lateral amalgamation of the channel-belt separates any formative channel centerline from the ridge centerline. Laterally-accreting bar strata are preserved. A random exhumation pattern not following the edges of the channel belt is unlikely to show any of these patterns.

170x127mm (300 x 300 DPI)

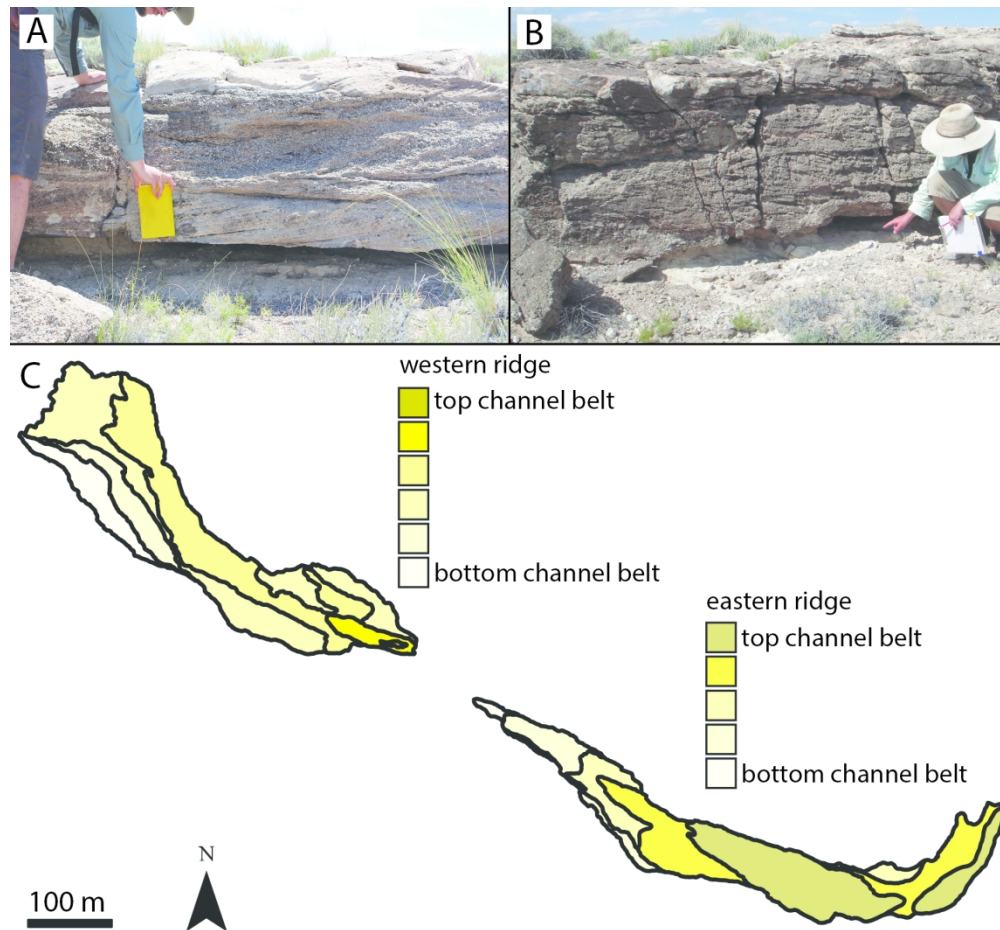


Figure 5 – (A-B) Beneath the yellow notebook (A) and at where the finger is pointing (B) are erosional surfaces associated with friable, recessed mudstones separating coarse-grained, cross-bedded packages. These erosional surfaces are interpreted to represent the contacts between stacked channel belts. Not all mudstones are associated with these surfaces. (C) Geologic maps showing the stacking patterns of channel belts exposed at the surface of both ridges. Darker yellows indicate higher stratigraphic positions. There is no attempt to correlate individual channel belts between ridges.

170x158mm (300 x 300 DPI)

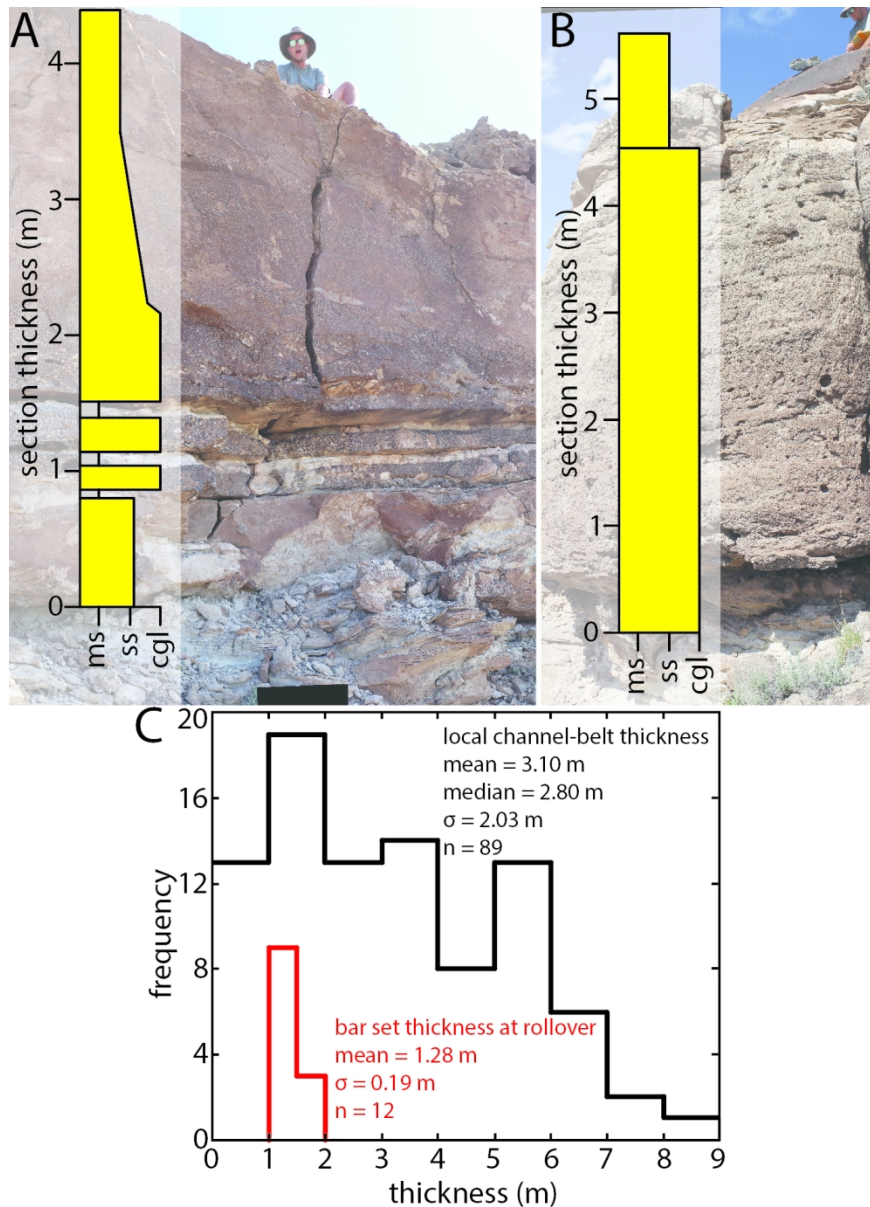


Figure 6 – (A) Vertical section showing story-bounding surfaces and associated mudstones. Stories in this section are of average to below-average thickness. (B) Two stories bounded by an erosional surface with no associated mudstone. The bottom story is above average thickness. (C) Histogram of local channel-belt (story) thicknesses measured from vertical sections, and the mean thickness of a bar set at the rollover (red line), which is used as a proxy for channel depth. The difference between channel depth and channel-belt thickness is due to aggradation of the channel bed.

119x165mm (300 x 300 DPI)

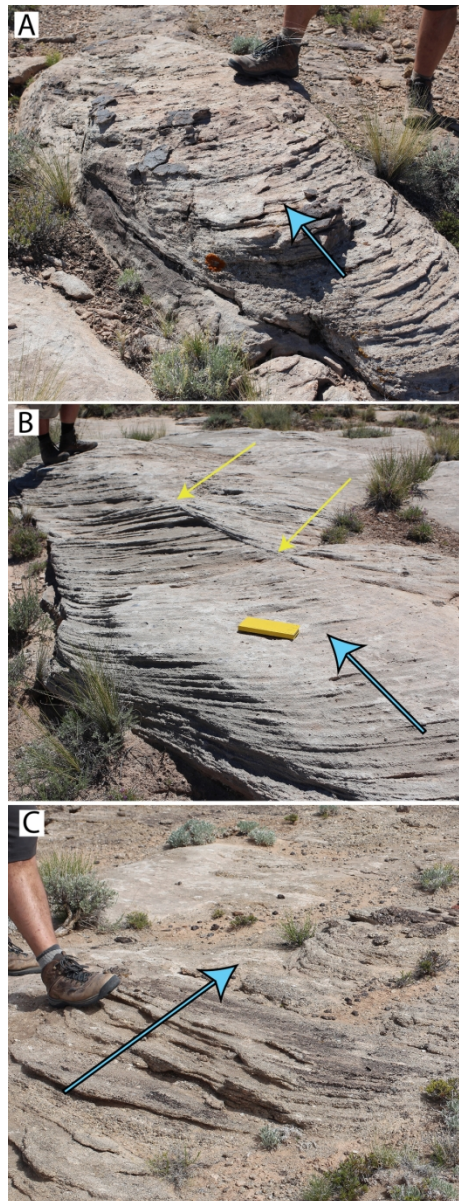


Figure 7 - Photos of cross strata exposed in planview along upper ridge surfaces. Teal arrows show the mean dip directions of cross strata. (A) This 3-D outcrop of a sandstone set shows the relationship between planform-exposed cross strata and vertically exposed cross strata. Boots for scale. (B) A 3-D exposure of a sandstone set. Yellow arrows point to the bounding surface separating two sets. This sort of amalgamation is common. Yellow field book for scale. (C) A conglomerate set showing minimal planform curvature. Boot for scale.

80x208mm (300 x 300 DPI)

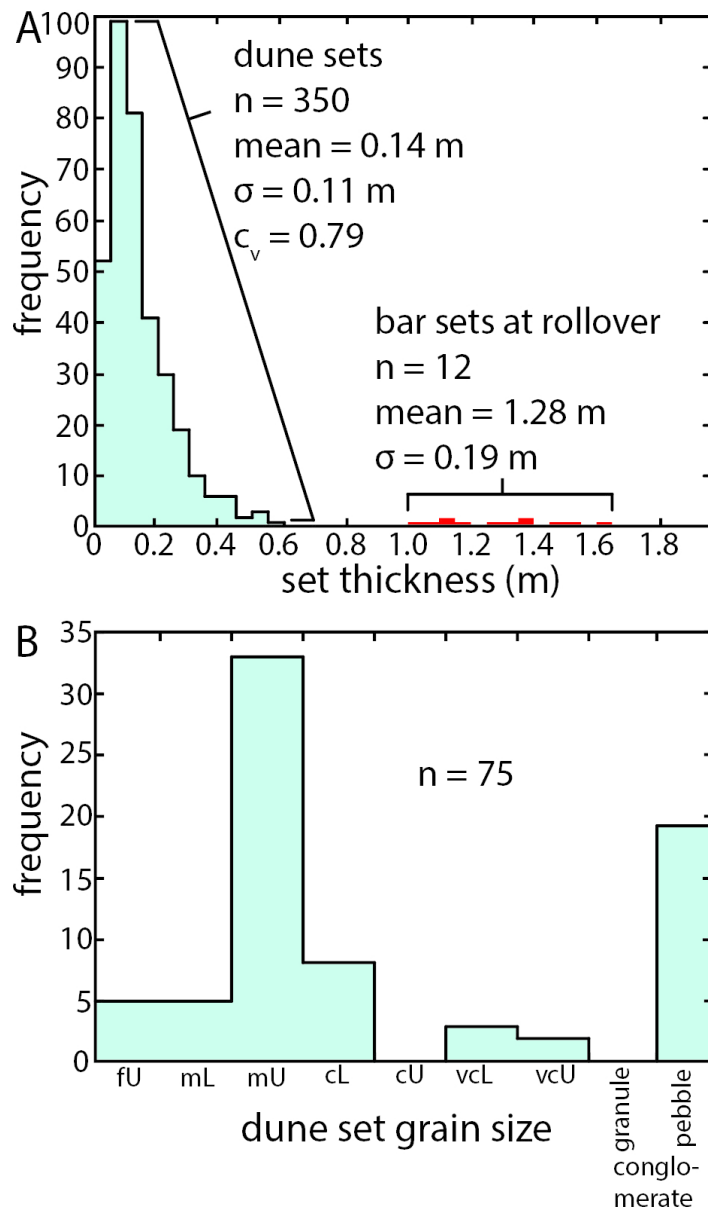


Figure 8 – (A) Teal histogram shows the distribution of the entire population of dune cross-set thicknesses, with statistical moments and the coefficient of variation (c_v). The distribution of bar set thicknesses at the rollover is shown in the red histogram. When measuring bar sets at the rollover, there is a break in the distribution of dune sets and bar sets. (B) Distribution of grain sizes of dune cross-sets. Measurements made in the field with a grain size card and hand lens.

80x134mm (300 x 300 DPI)

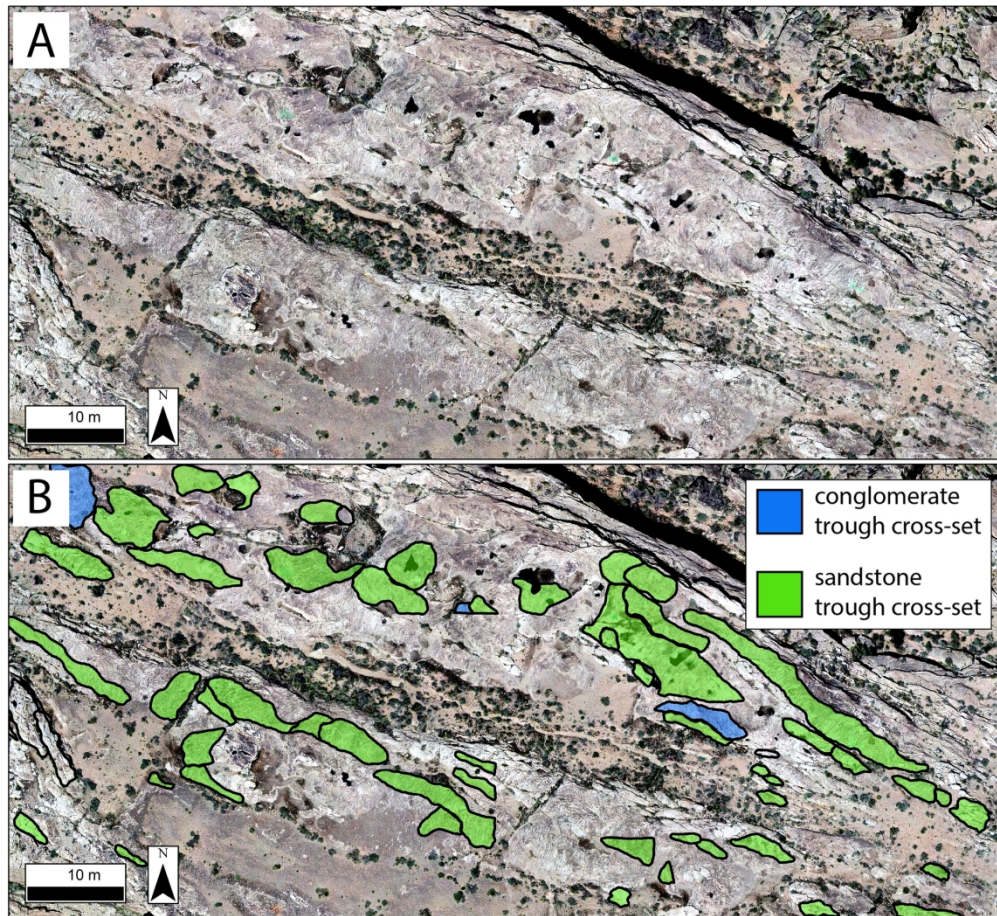


Figure 9 – (A) Example of uncrewed aerial vehicle photomosaics used as field base maps. (B) Digitized field map showing planform-exposed sets of cross strata outlined and filled in with green (sandstone) or blue (pebble conglomerate).

170x155mm (300 x 300 DPI)

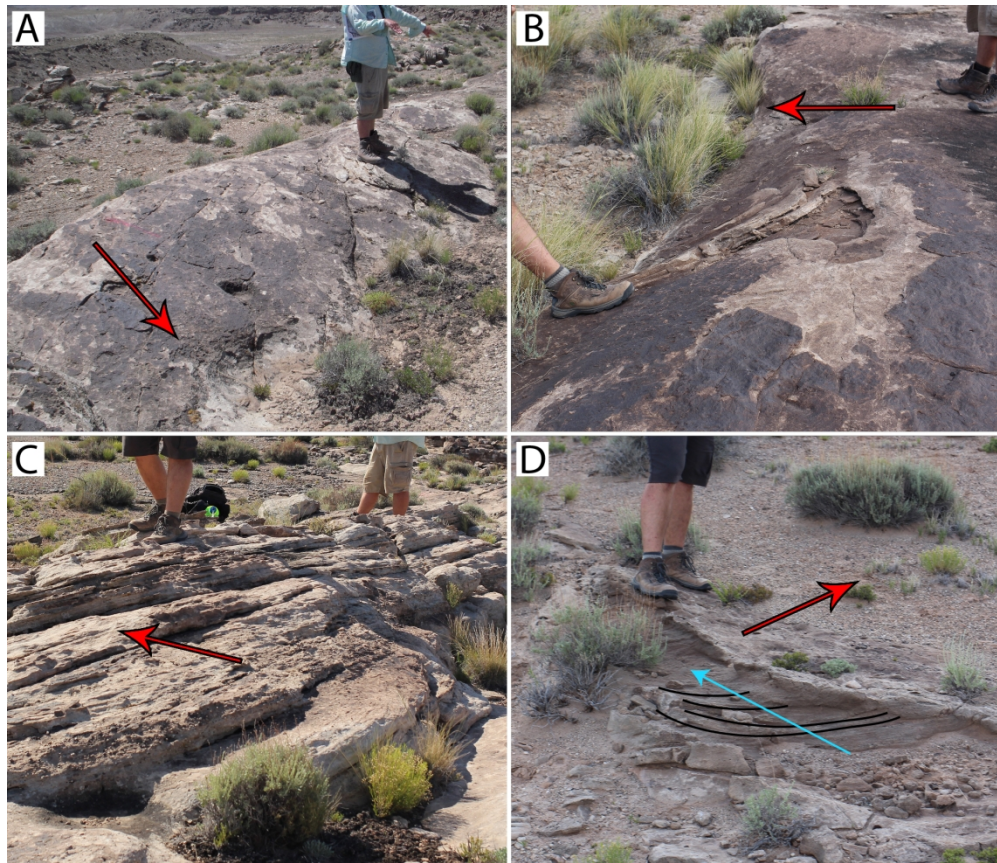


Figure 10 - Examples of larger-scale accretion strata in the field. Red arrows show the dip direction of the strata in each panel. (A) A typical example exposed for several meters. A lack of exposed bounding surfaces on this topographic surface suggests the topography itself represents a bounding surface. (B) Beneath the arrow, erosion exposes internal stratification parallel to the surface. (C) A 3-D outcrop of larger-scale dipping strata composed of smaller-scale stratification exposed by erosion. (D) Compound cross strata with a larger-scale accretion surface (red arrow) dipping obliquely to a smaller-scale dune set (teal arrow). A few dune cross strata are mapped in black lines.

170x146mm (300 x 300 DPI)

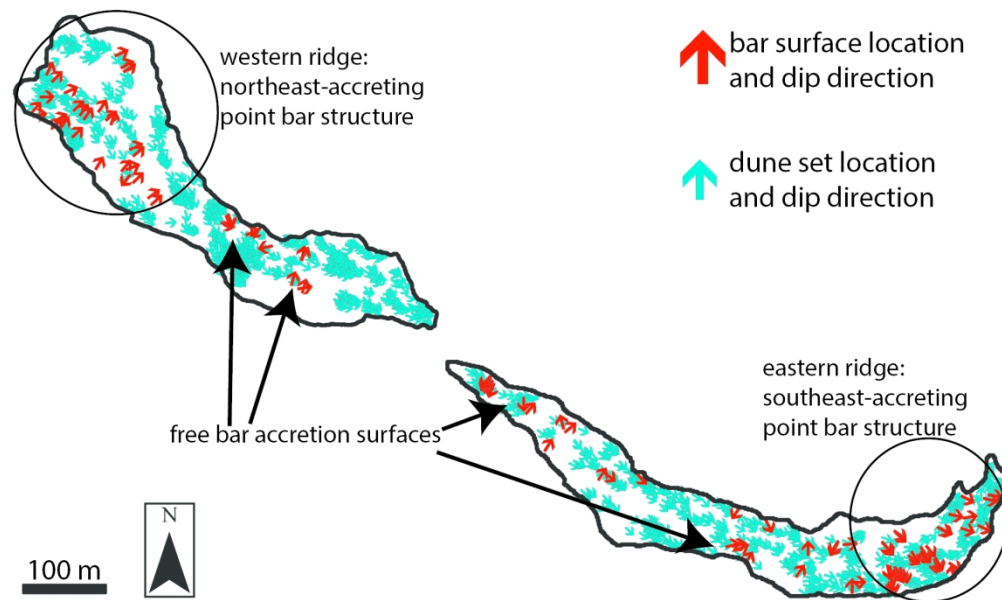


Figure 11 – Planform maps outlining the top surfaces of both studied ridges. Teal arrows show the locations of paleotransport measurements and point towards the measured direction. Red arrows show dip directions of large-scale dipping strata. Two locations with clusters of similarly-dipping bar accretion surfaces following ridge curvature are interpreted to represent point bars. The northeast-accreting point bar structure of the western ridge corresponds with a larger-scale ridge curvature beyond the extent of the study area (Fig. 1C). Bar accretion surfaces not clearly associated with a point bar are interpreted as free-bar accretion surfaces.

170x100mm (300 x 300 DPI)

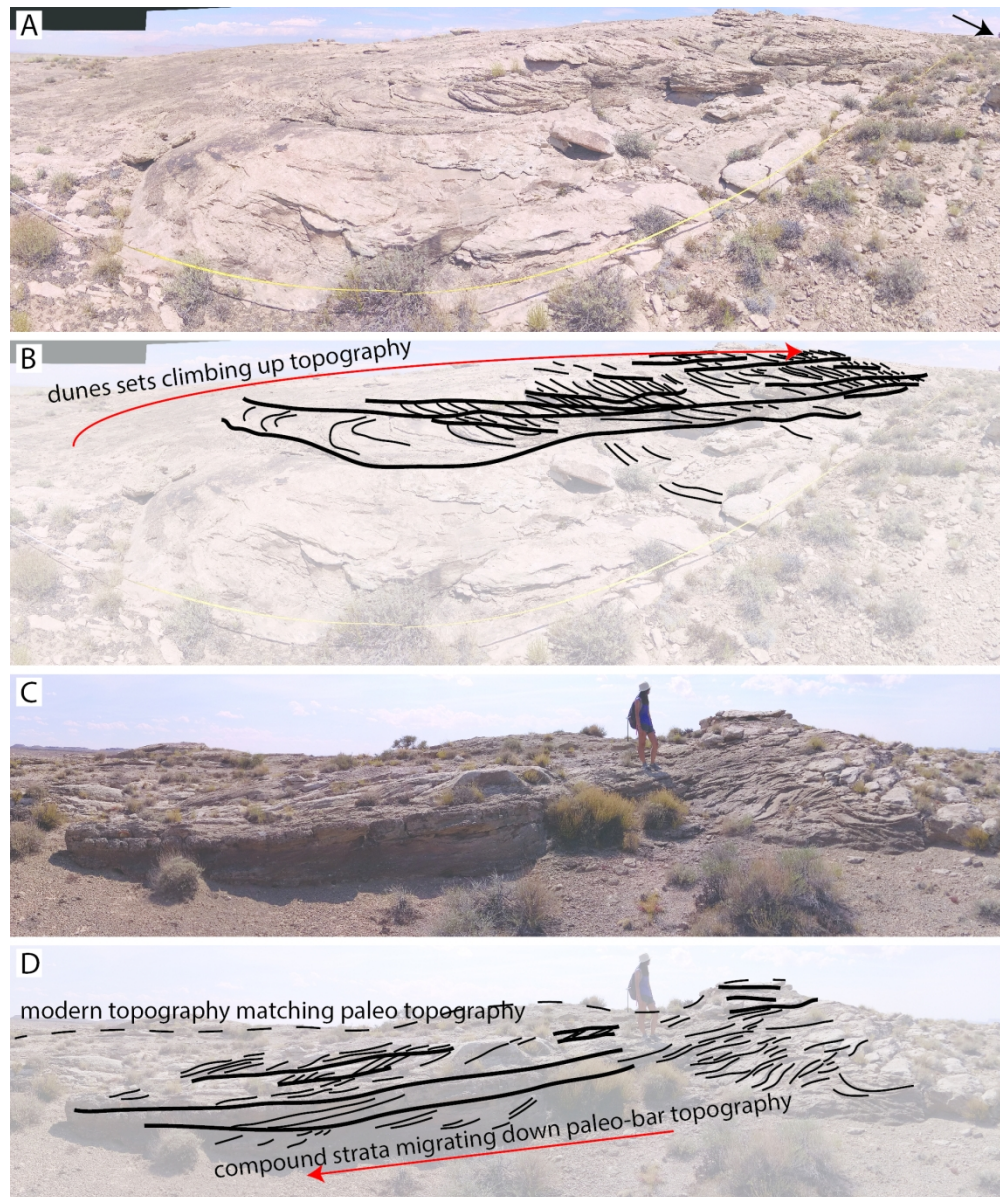


Figure 12 – The preservation of bar topography on upper-ridge surfaces. (A) Fisheye view of a sandstone mound rising towards the downstream direction (left to right), with a surface defined by shingled cross-sets climbing with topography. Interpreted as the stoss surface of a downstream-migrating barform. Tape measure for scale in foreground, arrow pointing to person in background. (B) Interpretation of panel A. (C) Downstream end of sandstone mound featuring cross sets and topography falling in the downstream direction. Interpreted as the lee slope of a downstream-migrating barform. Person for scale. (D) Interpretation of panel C. (E) Preserved point bar topography in the nearby Morrison Formation (Fig. 1B). In the foreground, the vertical exposure cuts through dune and bar stratigraphy, and clearly does not follow the paleo-topography of the bar. Contrast this with the steeper surface just beyond the vertical cut filling most of the background, which exposes shingled sets of planview-exposed dune cross sets. This surface approximates the original topography of the bar.

170x203mm (300 x 300 DPI)

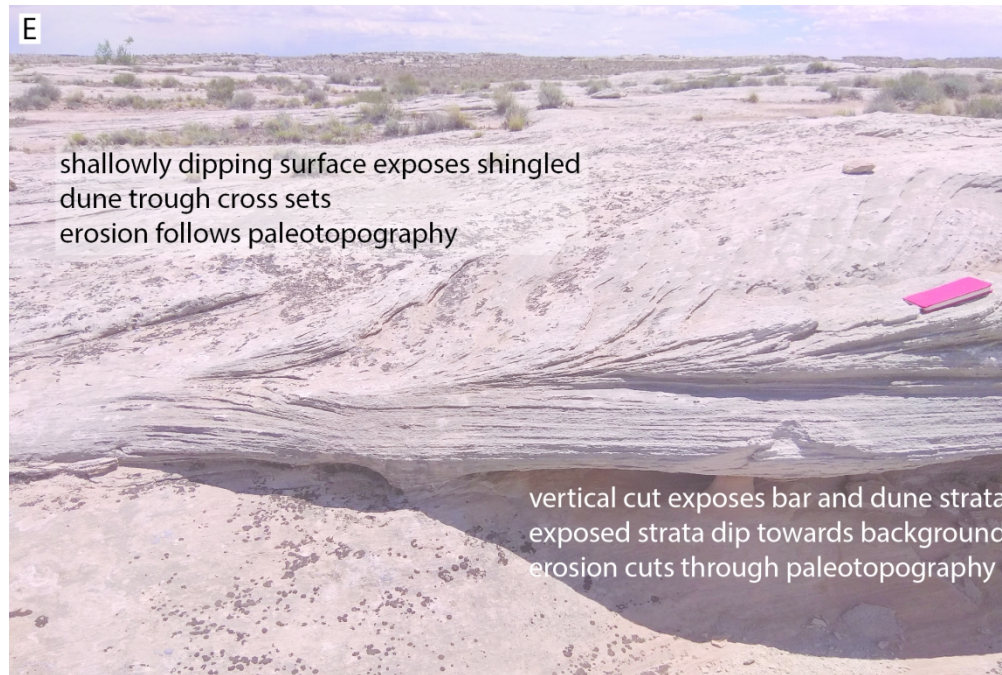


Figure 12 – The preservation of bar topography on upper-ridge surfaces. (A) Fisheye view of a sandstone mound rising towards the downstream direction (left to right), with a surface defined by shingled cross-sets climbing with topography. Interpreted as the stoss surface of a downstream-migrating barform. Tape measure for scale in foreground, arrow pointing to person in background. (B) Interpretation of panel A. (C) Downstream end of sandstone mound featuring cross sets and topography falling in the downstream direction. Interpreted as the lee slope of a downstream-migrating barform. Person for scale. (D) Interpretation of panel C. (E) Preserved point bar topography in the nearby Morrison Formation (Fig. 1B). In the foreground, the vertical exposure cuts through dune and bar stratigraphy, and clearly does not follow the paleo-topography of the bar. Contrast this with the steeper surface just beyond the vertical cut filling most of the background, which exposes shingled sets of planview-exposed dune cross sets. This surface approximates the original topography of the bar.

170x114mm (300 x 300 DPI)

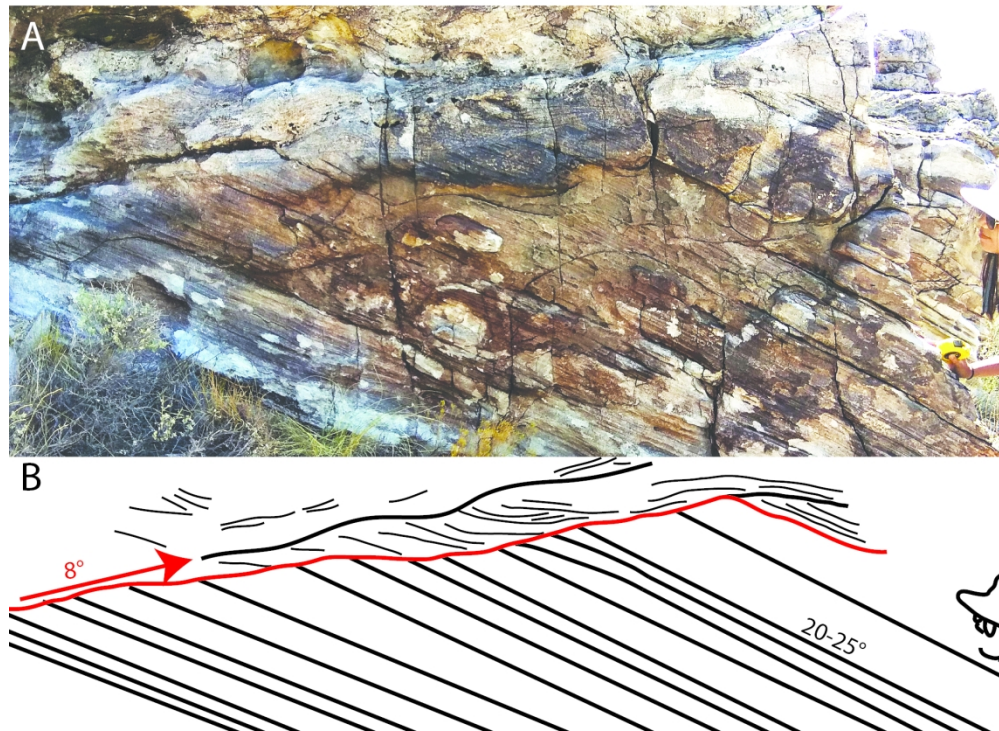


Figure 13 - Cross-sectional view of preserved strata from the stoss side of a bar, with an interpreted transition to the lee side. Flow was from left to right. In the sketch, the truncation surface separating lee-side (underneath) from stoss-side (above) strata is marked as a red line. This line is interpreted to preserve the upstream-dipping, stoss-side slope for the bar of 8° . Sets of dune strata are marked by thick black lines and dune cross strata by thinner black lines. Deposition on the stoss-side of the bar is best shown by the upward climbing dune sets at the left-side side of the panel. Beneath these stoss-side strata are steeply dipping beds recording the prior lee face of the bar. Towards the right-hand side of the photo, the truncation surface separating stoss and lee strata becomes conformable. The package of thick dune sets at this position is interpreted to be associated with higher sedimentation rates on the lee face of the bar. The observed spatial change in the dip angles of dune sets and the truncation surface document change in bar shape through time.

170x124mm (300 x 300 DPI)

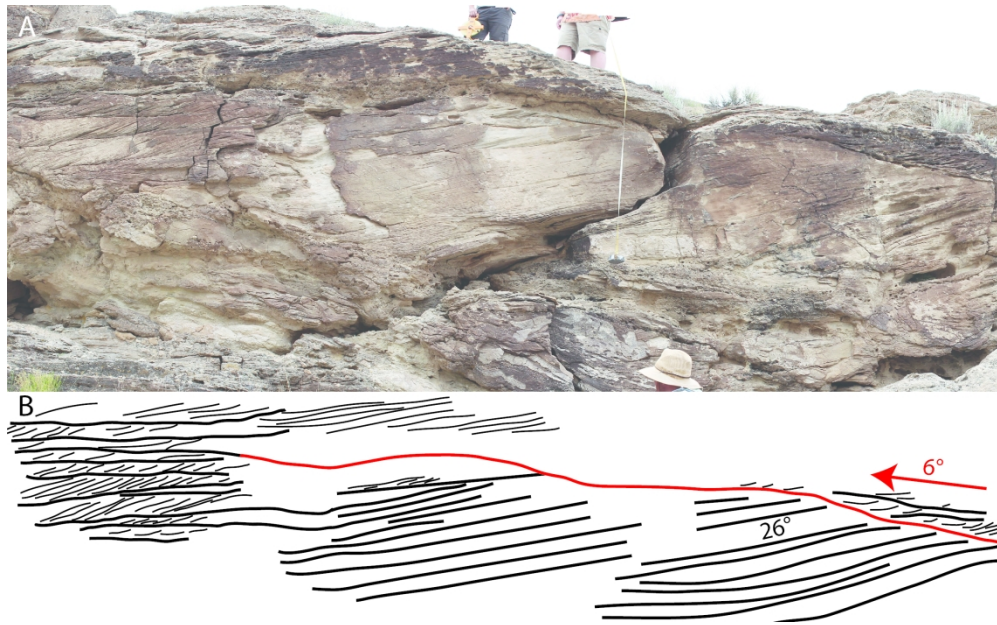


Figure 14 – Cross-sectional view of preserved strata from the lee and stoss sides of a bar form. Flow was from right to left. In the sketch, the truncation surface separating lee-side (underneath) from stoss-side (above) strata is marked as a red line. This line is interpreted to preserve the upstream-dipping, stoss-side slope for the bar of 6° . Sets of dune strata are marked by thick black lines and dune cross strata by thinner black lines. Deposition on the stoss-side of the bar is best shown by the upward climbing dune sets at the right-side side of the panel. Beneath these stoss-side strata are steeply dipping beds recording the prior lee face of the bar. At the left-hand side of the exposure it is particularly clear that the bar form is composed of compound strata in which the bar shape evolved through deposition of dune cross-beds. At this same location the truncation surface separating stoss and lee strata becomes conformable. The package of thick dune sets at this position is interpreted to be associated with higher sedimentation rates on the lee face of the bar. The observed spatial change in the dip angles of dune sets and the truncation surface document change in bar shape through time.

230x141mm (300 x 300 DPI)

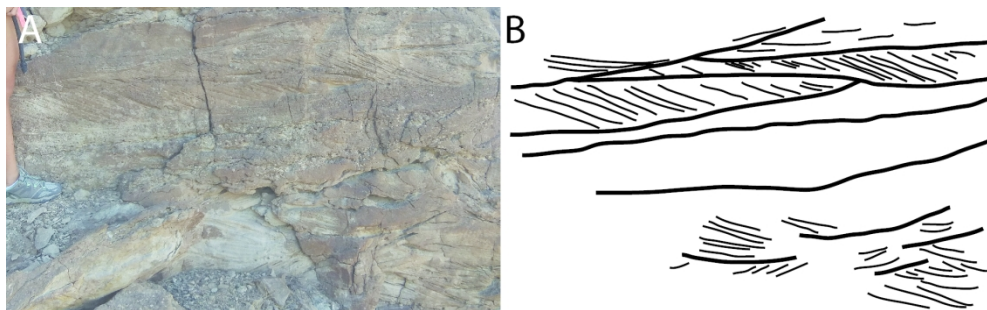


Figure 15 – Cross-sectional view of strata featuring a $\pm 90^\circ$ spread in transport direction, conglomerates, and a lack of bar architecture. This type of architecture is interpreted as a thalweg environment due to the coarser grains driven by higher velocity flow, and a larger spread in transport driven by changes in steering due to bar growth. The sketch shows bounding surfaces and cross strata.

170x51mm (300 x 300 DPI)

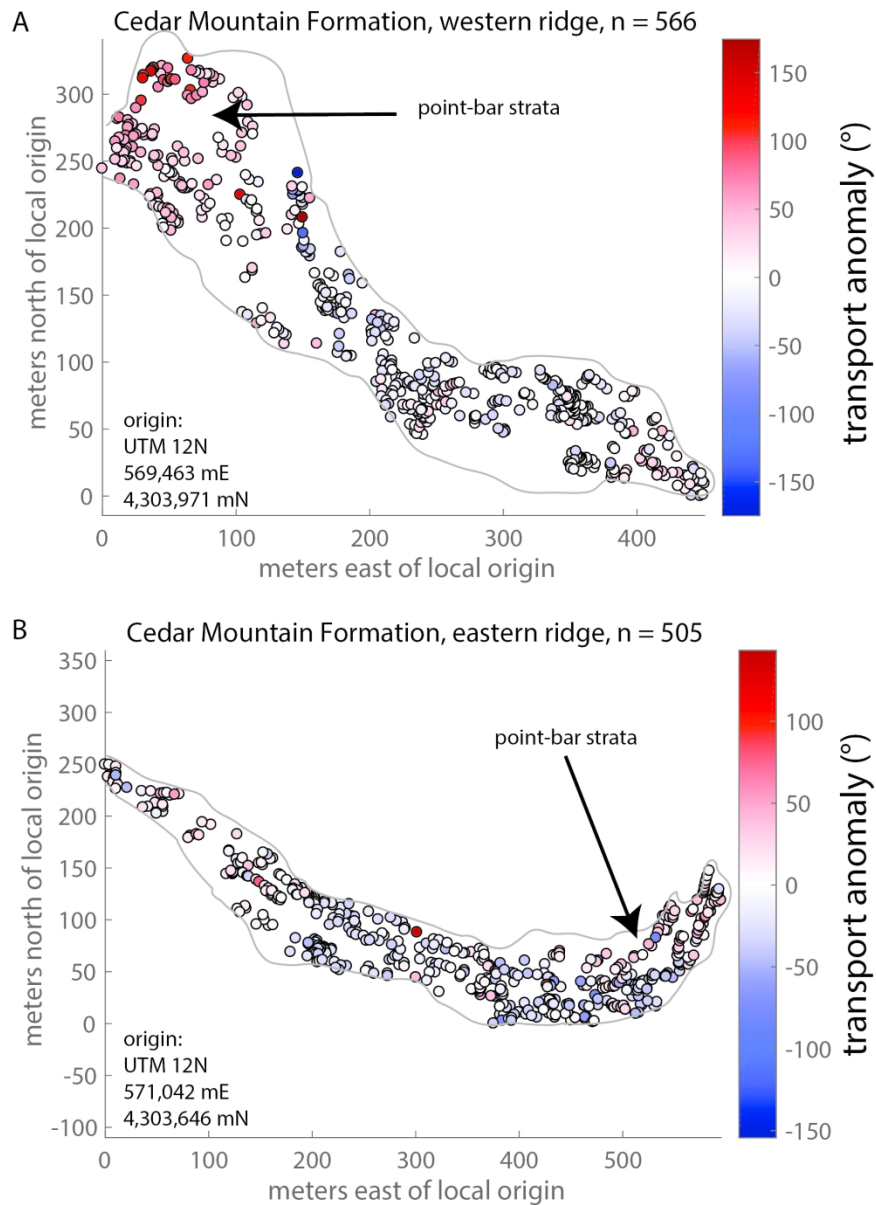


Figure 16 – Transport anomaly maps of the western ridge of the Cedar Mountain Formation (A), the eastern ridge (B), and the North Loup River (C). X and Y coordinates are relative to a different local datum in each map, shown in the bottom left corner of each panel. Circles show the location of paleotransport or modern transport direction measurements. The color at each point represents the paleotransport or transport anomaly (Fig. 3A-B). Gray lines represent ridge outlines and the banks of the North Loup River. Black arrows in panels A and B point to regions recording point bar accretion, and are associated with relatively high anomaly values, particularly in the western ridge (Figs. 1C and 11).

170x230mm (300 x 300 DPI)

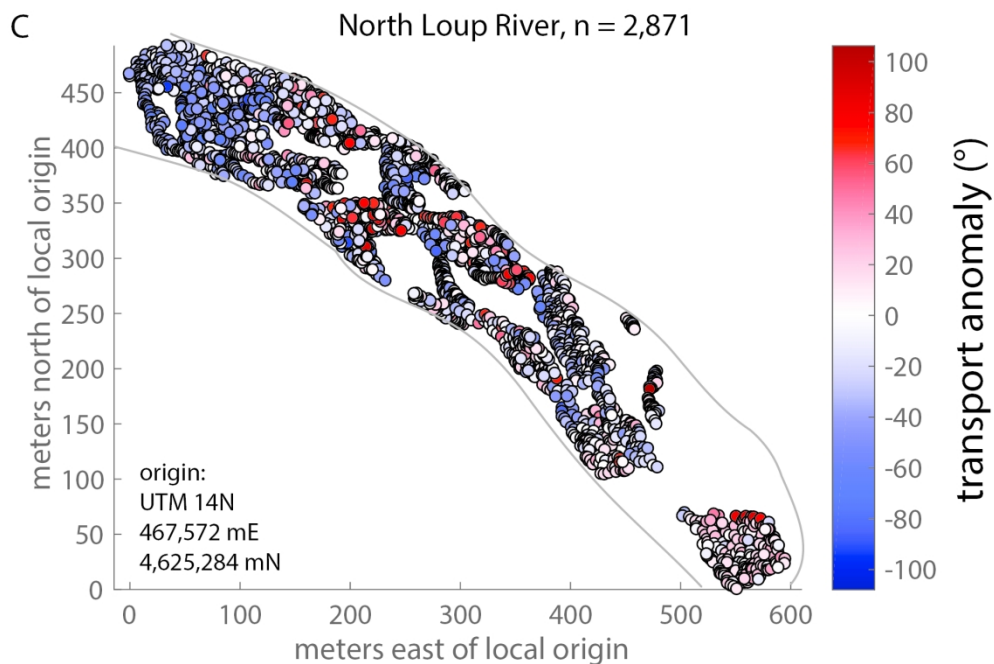


Figure 16 – Transport anomaly maps of the western ridge of the Cedar Mountain Formation (A), the eastern ridge (B), and the North Loup River (C). X and Y coordinates are relative to a different local datum in each map, shown in the bottom left corner of each panel. Circles show the location of paleotransport or modern transport direction measurements. The color at each point represents the paleotransport or transport anomaly (Fig. 3A-B). Gray lines represent ridge outlines and the banks of the North Loup River. Black arrows in panels A and B point to regions recording point bar accretion, and are associated with relatively high anomaly values, particularly in the western ridge (Figs. 1C and 11).

170x112mm (300 x 300 DPI)

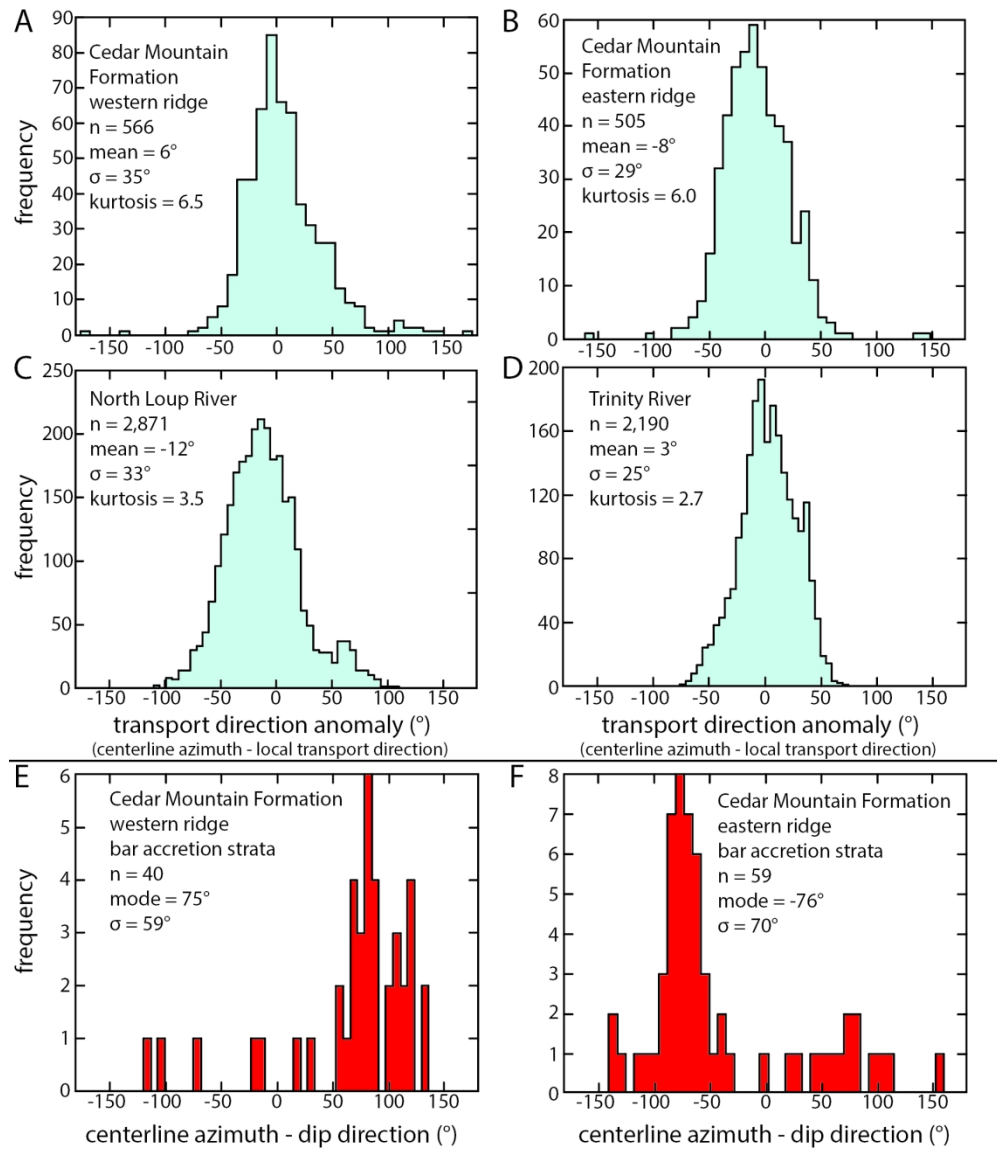


Figure 17 – Histograms showing the distribution of paleotransport/transport anomalies of the western (A) and eastern (B) ridges of the Cedar Mountain Formation, and the modern North Loup River (C) and Trinity River (D). The number of measurements, mean, and standard deviation are reported in each panel. Note the similarity in mean and standard deviation between the ancient and modern datasets. Histograms (D) and (E) show the difference between dip directions of bar accretion strata exposed along the upper surfaces of ridges and the centerline. Both histograms show a wide distribution of values with peaks approaching perpendicular to the centerline trend.

170x193mm (300 x 300 DPI)

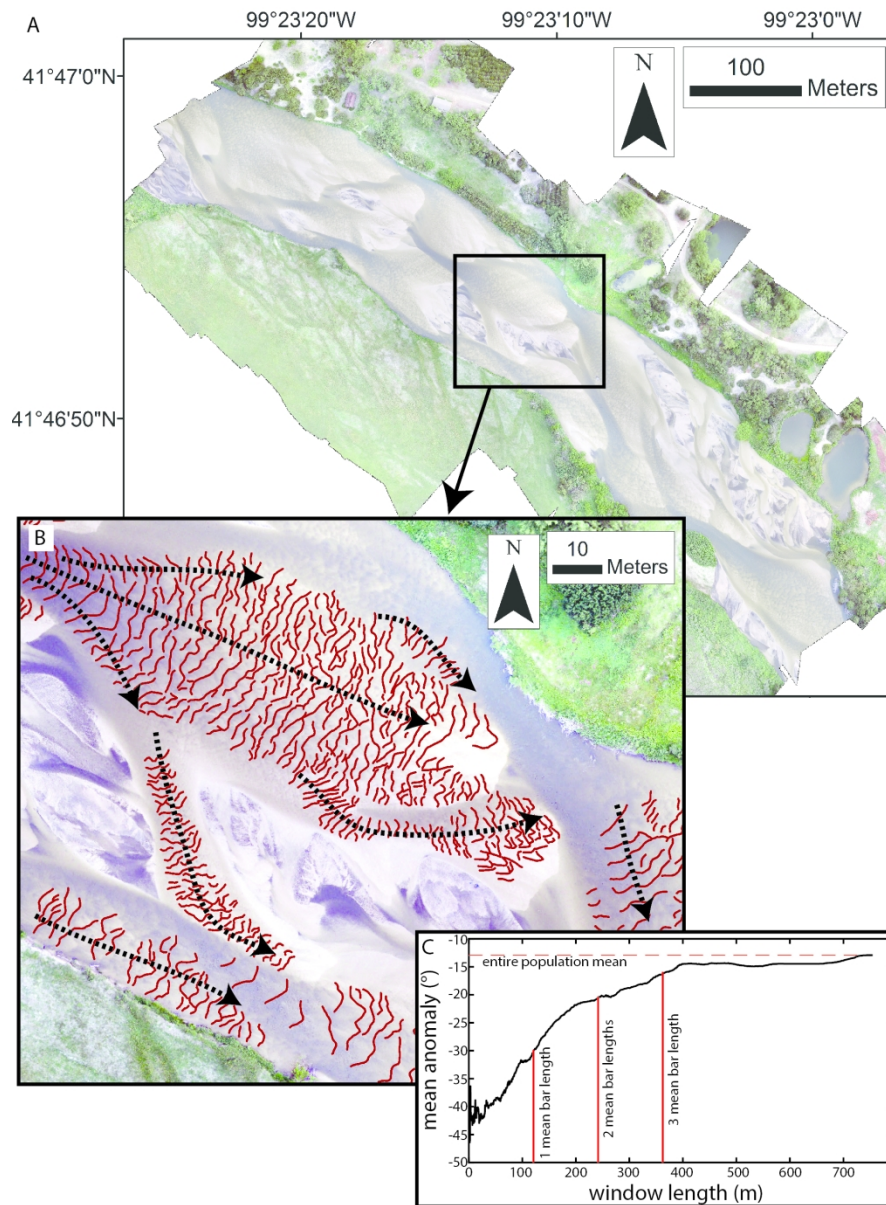


Figure 18 – (A) Drone photomosaic of the North Loup River near Taylor, Nebraska, USA (Swanson et al., 2018). Brighter tan colors within the channel are subaqueous and represent higher portions of downstream-migrating bars beneath shallow water. Darker reaches of the channel represent deeper water. Mixed white and black areas with no crestlines mapped are subaerially exposed bar tops that are not currently undergoing fluvial transport. The location of panel B is shown in the black box. (B) Zoom in showing dune crestlines (short red lines) interpreted as perpendicular to dune transport direction. Black dashed arrows show general trends in local transport directions due to the steering of flow around bars. (C) Window length vs. the mean transport anomaly within the window. As the window length approaches that of the ~ 3 barforms, the sampled mean approaches the mean of the entire dataset. Changes in curvature of this line happen near multiples of mean bar length (red vertical lines), supporting topographic steering as the source of the transport anomaly.

170x230mm (300 x 300 DPI)

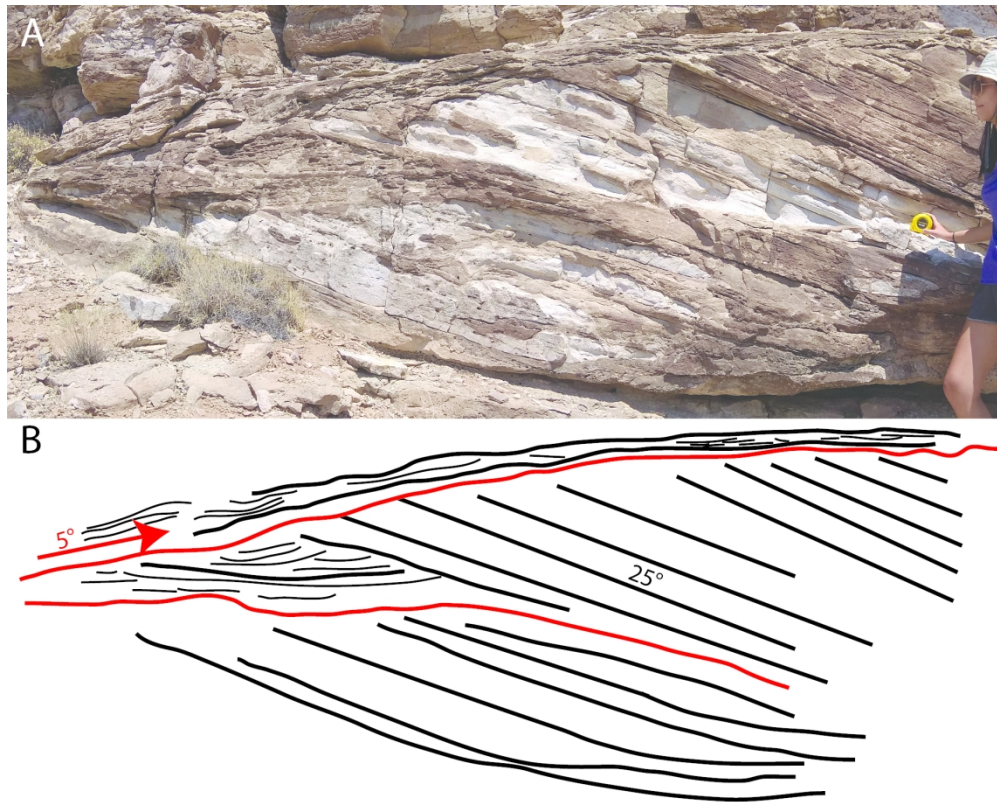


Figure 19 – Cross-sectional view showing the internal structure of a barform. Flow was from left to right. In the sketch, the bottom-most red line marks a surface at which lower bar-scale cross strata are truncated. This surface becomes conformable with the bar strata downstream, and features a veneer of smaller-scale sets above it. This arrangement is consistent with a bar stoss-to-lee transition. The upper-most red line defines a 5° upstream-dipping surface truncating 25° downstream dipping bar-scale strata. Above this surface are two dune-scale sets. The architecture arranged around this red surface is consistent with a bar stoss environment. From bottom to top, the transition from stoss-to-lee architecture to lee architecture, all within the same barform, records the forward migration and aggradation of the barform.

170x136mm (300 x 300 DPI)

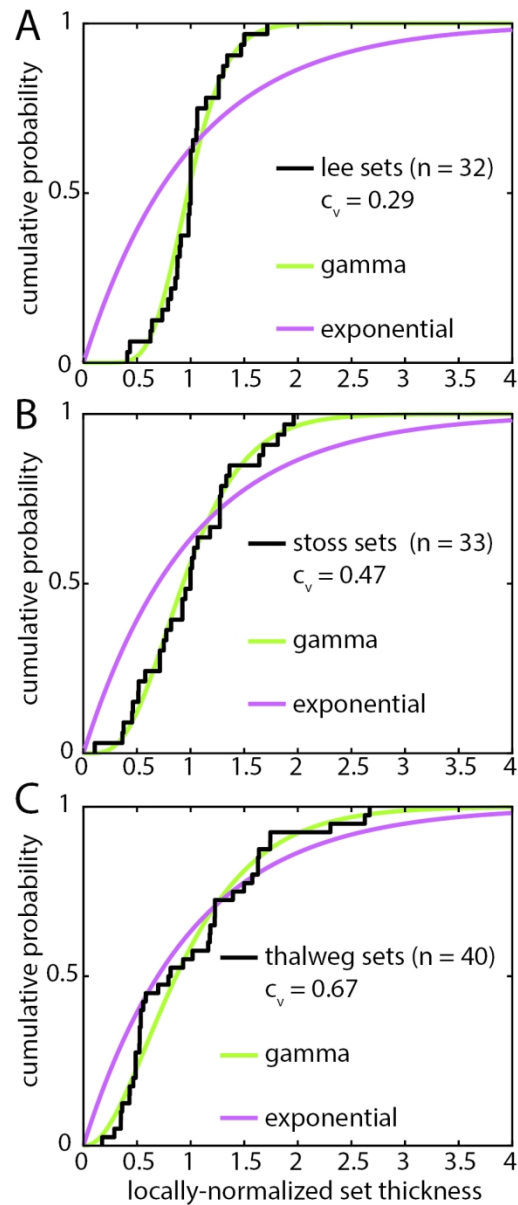


Figure 20 – (A) Cumulative distribution function (CDF) showing the mean-normalized distribution of set thickness located within bar lee environments (Fig. 14). (B) CDF of set thickness within bar stoss environments (Fig. 13). (C) CDF of thalweg set thickness (Fig. 15). The best-fit gamma and exponential curves are shown for each distribution. In all cases, the exponential fits are rejected using a Kalmogorov-Smirnov test at a significance level of .05, and the gamma fits are not. This suggests all architectures required a significant rate of bed aggradation relative to the rate of dune migration, although the similarity of the two curves for thalweg sets indicates the ratio of bed aggradation to dune migration was the lowest of the three environments (Paola and Borgman, 1991; Jerolmack and Mohrig, 2005).

80x188mm (300 x 300 DPI)

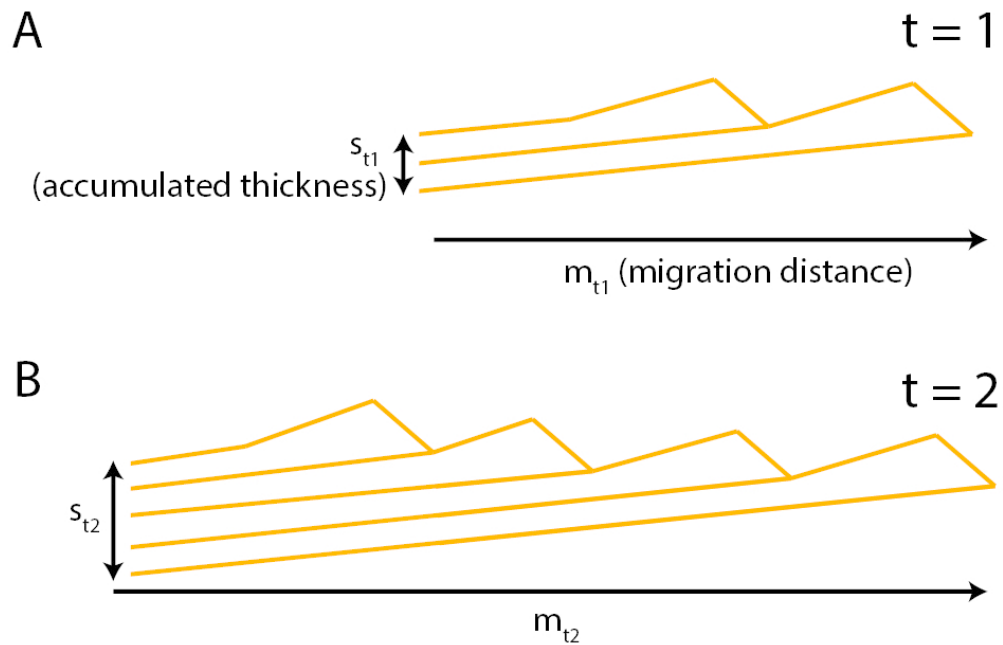


Figure 21 – A diagram explaining the calculation of accumulation time of dune cosets with thickness s , assuming continuous transport (Eqs. 2-5). Dune cosets may be located on bars or the thalweg. Dune migration is towards the right. (A) At $t = 1$, dunes with a given ratio of aggradation rate (r) to migration rate (c) migrate a distance of mt_1 , leaving a deposit of thickness st_1 . (B) At $t = 2$, this process has continued with the same r and c . Dunes have migrated a farther distance, mt_2 , accumulating a thicker coset package, st_2 .

80x52mm (300 x 300 DPI)

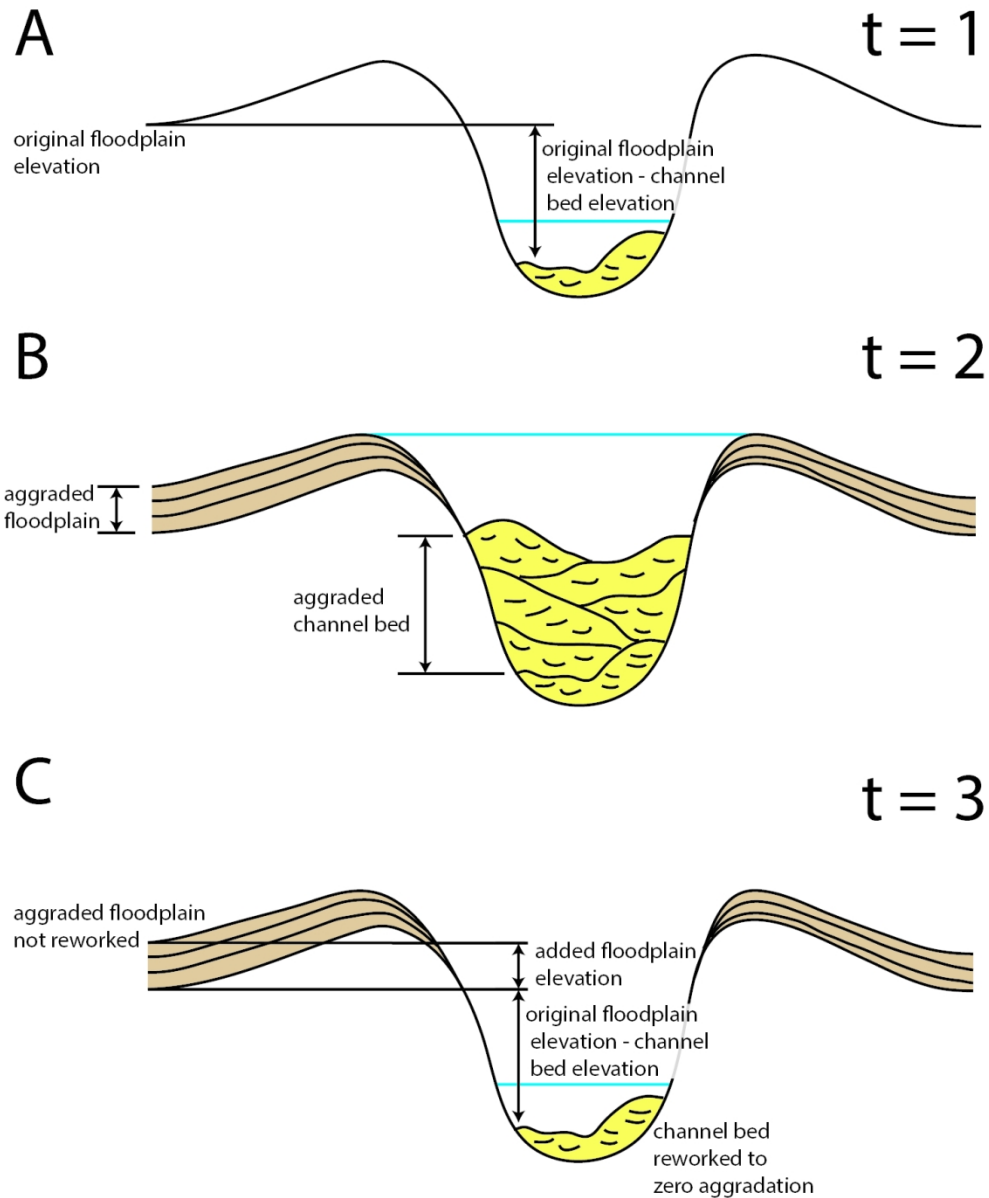


Figure 22 – A diagram merging the observations of the usually bypass-state channel bed and the relatively high amount of channel-bed aggradation preceding avulsion, when compared to other fluvial strata (e.g., Mohrig et al., 2000). (A) at $t = 1$, the distance between the lowest part of the floodplain and the channel bed during low flow is defined. (B) At $t = 2$, the channel is in flood stage. The floodplain has aggraded less than the channel bed. Avulsion does not occur. (C) At $t = 3$, the channel bed has been reworked to the configuration of $t = 1$, maintaining its net-sediment bypass state. The floodplain has not been reworked. Thus, the vertical distance between the channel bed and the lowest part of the floodplain has increased. On average, more channel-bed aggradation will be required to set up an avulsion.

122x149mm (300 x 300 DPI)